The stress field in Europe: optimal orientations with confidence limits

M. M. C. Carafa[1] and S Barba[2]

Istituto Nazionale di Geofisica e Vulcanologia.

[1] L'Aquila, Italy. E-mail: michele.carafa@ingv.it

[2] Rome, Italy. E-mail: salvatore.barba@ingv.it

Cite as: Carafa, M. M. C. & Barba, S., 2013. The stress field in Europe: optimal orientations with confidence limits, Geophys. J. Int., doi: 10.1093/gji/ggt024

First published online: February 19, 2013.

Summary

In this study, we modify and extend a data analysis technique to determine the stress orientations between data clusters by adding an additional constraint governing the probability algorithm. We apply this technique to produce a map of the maximum horizontal compressive stress (S_{Hmax}) orientations in the greater European region (including Europe, Turkey and Mediterranean Africa). Using the World Stress Map dataset release 2008, we obtain analytical probability distributions of the directional differences as a function of the angular distance, θ. We then multiply the probability distributions that are based on pre-averaged data within $\theta < 3°$ of the interpolation point and determine the maximum likelihood estimate of the S_{Hmax} orientation. At a given distance, the probability of obtaining a particular discrepancy decreases exponentially with discrepancy. By exploiting this feature observed in the World Stress Map release 2008 dataset, we increase the robustness of our S_{Hmax} determinations. For a reliable determination of the most likely S_{Hmax} orientation, we require that 90% confidence limits be less than ±60° and a minimum of three clusters, which is achieved for 57% of the study area, with small uncertainties of less than ±10° for 7% of the area. When the data density exceeds 0.8×10^{-3} data/km^2, our method provides a means of reproducing significant local patterns in the stress field. Several mountain ranges in the Mediterranean display 90° changes in the S_{Hmax} orientation from their crests (which often experience normal faulting) and their foothills (which often experience thrust faulting). This pattern constrains the tectonic stresses to a magnitude similar to that of the topographic stresses.

Keywords: Neotectonics; Seismicity and tectonics; Fractures and faults; Intra-plate processes; Plate motions; Dynamics: gravity and tectonics.

1. Introduction

This study aims to exploit the high data density of the World Stress Map release 2008 (hereinafter, WSM08) (Heidbach *et al.*, 2008) in the greater European region (including Europe, Turkey and Mediterranean Africa) to gain additional information on short-wavelength stress sources. Knowledge of the local stress field helps to identify potential slip on pre-existing favourably oriented fault planes (e.g., Sibson et al., 2011; Syracuse et al., 2012) and has an impact on seismic hazard assessment, geodynamics, hydrocarbon exploitation, and global-to-regional–scale tectonics (Carafa & Barba, 2011; Herget & Heidbach, 2011; Ghisetti & Sibson, 2012). However, interpolating or smoothing the stress orientations of clustered and scattered data requires several assumptions and approximations.

Rebai *et al.* (1992) studied the irregular spatial distribution of stress data by determining the maximum horizontal compressive stress (S_{Hmax}) orientations on an irregular triangular element grid with the locations of grid nodes dependent upon the spatial distribution of the data. For clusters, the nodes were collocated at the centre, whereas for sparse data, the nodes were placed at data locations. At each node, Rebai *et al.* (1992) computed an average S_{Hmax} orientation by smoothing the S_{Hmax} data within a specified distance from the node. This distance was assumed to be proportional to the size of the smallest triangle connected to the node. The S_{Hmax} average was weighted by the quality factor assigned to the stress datum and by the scale factor associated with the type of S_{Hmax} indicator (decimetres to metres for borehole breakouts, kilometres for focal mechanisms). Within the triangular elements, the nodal values were linearly interpolated.

Lee & Angelier (1994) reconstructed the 2D regional principal palaeostress axis orientations using two different approaches. In the first approach, the stress orientations were represented by a polynomial function of flat-Earth coordinates. The coefficients of the polynomial were determined using weighted least-squares to fit the measured S_{Hmax} orientations, with the weight of each S_{Hmax} datum dependent upon its uncertainty. In the second approach, the S_{Hmax} data were also weighted by a power-law function of the distance. The second approach provided better results, indicating that proper distance weighting is essential in stress interpolation.

Coblentz & Richardson (1995) quantified long-wavelength trends in the global S_{Hmax} orientations and stress regime patterns using the World Stress Map database release 1992 (hereinafter, WSM92;

Zoback, 1992). The authors binned the S_{Hmax} data into 582 5°×5° cells. Of the 382 bins containing at least two S_{Hmax} orientations, Coblentz & Richardson (1995) estimated which bins had non-random S_{Hmax} orientations with standard deviation <25° by employing a Rayleigh test at the 90%, 95%, and 97.5% confidence levels. The test assumes that random S_{Hmax} orientations follow a von Mises normal distribution (Mardia, 1972). The hypothesis that stress orientations are random in WSM92 was rejected at the 97.5% confidence level for 197 out of 382 bins, suggesting that large portions of intra-plate regions have coherent S_{Hmax} orientations and are primarily in a state of compression.

Assuming two-point conditional probabilities, Bird & Li (1996) empirically determined the probability distributions of the angular differences (also called discrepancies) in the S_{Hmax} orientations based on WSM92 data. They used two approaches: one that accounted for the quality factor and one in which the clustered data were pre-averaged. Although both concepts are important, they have not yet been implemented simultaneously. Neglecting the quality factor results in the underweighting of the most accurate data, whereas when clustered data are used, the uneven data sampling causes a loss of precision that is not easily included in the error estimates.

Müller *et al.* (2003) determined the S_{Hmax} orientations using the nearest-neighbour regression method. The authors compared two approaches using either a fixed search radius or a fixed number of nearest neighbours. The smoothing was performed at grid points, with the data weighted by both quality and distance. In particular, the quality weight was 1 for rank A, 0.75 for rank B, 0.5 for rank C, and 0 for ranks D and E (see Zoback (1992) for a description of the quality factors). The distance weight was expressed as a tricube weight function:

$$w(x, x_i) = \begin{cases} \left[1 - \left(\frac{\|x - x_i\|}{R}\right)^3\right]^3 & for \ \|x - x_i\| < R, \\ 0 & otherwise \end{cases}$$

where x_i is the position of the *i*th data point and R is either the fixed search radius or the distance to the (N+1)-th nearest neighbour. Müller *et al.* (2003) performed checkerboard-like synthetic tests and verified that using a fixed search radius is preferable for recovering the stress domains. To avoid interpolating stress orientations in areas of poor data coverage, minimum threshold values for the sum of the quality and distance weights were suggested. The approach of Müller *et al.* (2003) proved to be flexible and capable of providing an empirical model of the stress processes. However, this approach is sensitive to outliers and suffers when the data density is low.

Rather than using discrete weights, several groups (e.g., Hardebeck & Michael, 2006; Arnold & Townend, 2007) have developed methods to propagate observational errors as formal uncertainties in S_{Hmax}, which comprise mainly focal mechanisms. Hardebeck & Michael (2006) used a damped inversion method to determine stress on a grid, which minimises the difference between adjacent

97 points. The damped inversion removes the stress rotation artefacts exhibited by undamped
98 inversions and resolves stress rotations better than moving-window approaches. Arnold & Townend
99 (2007) developed a Bayesian formulation for estimating tectonic stress orientations, which
100 combines a geologically based prior stress model and focal mechanism observations, including their
101 precisions. Their technique produces the posterior density function of the principal components of
102 the stress tensor and of the stress-magnitude ratio, which have been used to determine S_{Hmax}
103 following the approach of Lund & Townend (2007).
104 Heidbach *et al.* (2010) calculated the global S_{Hmax} orientations by smoothing stress data that were
105 weighted by both quality and distance. The distance weighting function was $min(1/D\,, 1/20\,km)$,
106 where D is the distance between the data location and grid point and min represents the minimum of
107 the two arguments. The quality weights were 1/15, 1/20, and 1/25 for A-, B-, and C-quality data,
108 respectively. The S_{Hmax} orientations were defined if there were at least five WSM08 data within the
109 variable search radius and if the weighted standard deviation was ≤25°. Pierdominici & Heidbach
110 (2012) introduced an additional condition that the data be located in two diagonal quadrants, with at
111 least 10 WSM08 data within the search radius. No constraints were placed on the standard deviation
112 in their study.
113 In this paper, we aim to address three major issues that have not previously been resolved
114 simultaneously: the scatter in S_{Hmax} orientations, the uneven sampling of stress data, and the
115 correlation of stress orientations with distance. We modified and extended the clustered data
116 analysis technique used by Bird & Li (1996) by adding a constraint governing the probability
117 algorithm for estimating S_{Hmax} orientations. Given the intrinsically clustered nature of earthquakes
118 and the uneven sampling of boreholes, we pre-averaged clustered data and updated the empirical
119 probability distributions using the WSM08. In agreement with the data, we modelled the
120 probabilities as exponentially decreasing with discrepancy, thereby compensating for the low data
121 density. An S_{Hmax} orientation was assigned to each interpolation point if three conditions were
122 satisfied: a) a minimum of three clusters; b) 90% confidence limits less than ±60°; and c) a
123 maximum search radius of 327 km.
124 The resulting stress maps have 90% confidence limits of less than ±45° for 38% of the study area
125 and uncertainties of less than ±30° for the 19%. The results presented in this work cover 57% of the
126 entire study area. Our S_{Hmax} orientations overlap with 28% of those in Heidbach *et al.* (2010); the
127 spatial distributions of the two stress fields are therefore complementary. Where the two maps
128 overlap, the results differ by more than 30° for only 2% of our study area. The stress orientations
129 determined using our method are generally consistent with the S_{Hmax} orientations obtained using
130 geological indicators, earthquakes, and numerical models. Our method is able to detect several

small-scale (20-50 km) stress perturbations, thereby better constraining and complementing the stress field determinations available elsewhere in the literature.

2. Data and method

Based on previous studies of stress interpolation, the angular differences (discrepancies) between two S_{Hmax} orientations tend to increase with distance or, alternatively, the closest S_{Hmax} datum to an interpolation point is weighted most heavily. Of the various data weighting algorithms suggested in the literature, we adopted the approach of Bird & Li (1996). In this approach, S_{Hmax} is determined at each integration point using two-point conditional probabilities and assuming all of the WMS08 data to be independent. The conditional probability of an event is the probability of that event occurring given that another event has already occurred. In terms of conditional probabilities, the S_{Hmax} orientation represents the azimuth with the highest probability of occurring given the neighbouring WSM08 data. We defined the empirical two-point conditional probability based on the stress data (see subsection 2.1) and the analytical probability using least-squares fitting (subsection 2.2). We then used the declustering method of Bird & Li (1996) and the analytical probabilities to determine the S_{Hmax} orientations. We applied our method to study short-wavelength patterns over a wide area (total extent of 2.7×10^{9} km^2) from 30W to 40E longitude and 25N to 76N latitude, roughly corresponding to the geographic location of the greater European region.

2.1. Data

We used the S_{Hmax} data records from the WSM08 dataset (http://www.world-stress-map.org). Each stress datum was assigned a quality factor between A and E, with A being the highest quality and E the lowest. The standard deviations of A-, B-, C-, and D-quality data records are within ±15°, ±20°, ±25°, and ±40°, respectively. E-quality data records have standard deviations greater than 40°. The WSM08 dataset consists of 21,750 data records, of which 16,961 have qualities of A-C; these data form approximately 1.4×10^{8} unique pairs, representing a significant improvement over the 1.8×10^{7} data pairs obtained by Bird & Li (1996) using WSM92. The data density increased from 0.012×10^{-3} data/km^2 in WSM92 to 0.041×10^{-3} data/km^2 (0.033×10^{-3} data/km^2 for A-, B-, and C-quality data) in WSM08. North America, Europe, and China are the most densely sampled zones. Within Europe, Italy and Switzerland have the highest data densities, with an average of 3×10^{-3} data/km^2 (Fig. 1). However, many locations in Anatolia, the Hellenic Arc, the Pyrenees, Northwestern Europe, and the North Sea have densities exceeding 0.7×10^{-3} data/km^2.

2.2. Empirical probabilities

The angle between any pair (r,s) of S_{Hmax} data points on Earth is the discrepancy β defined by Bird & Li (1996) as follows:

$$\beta = \min_{m=-3}^{+3} |\alpha_r - \gamma_r + \gamma_s - \alpha_s + m \times 180°|, \quad (1)$$

where m is an integer between -3 and 3, γ_r and γ_s are the local azimuths of the great circle connecting the two data points, and α_r and α_s are the S_{Hmax} azimuths relative to North (Fig. 2). Our first step was to determine the number of WSM08 pairs as a function of the discrepancy β and range (or angular distance) θ. Following Bird & Li (1996), we used 30 3°-wide sectors for β and 150 concentric annuli for θ. The annulus *n* is defined such that $\theta_{n-1} \leq \theta < \theta_n$, with

$$\boldsymbol{\theta_n \cong cos^{-1}\{1 - 2(n/150)^{1/(1-\varepsilon)}\}}. \quad (2)$$

The WSM08 dataset is 3.5 times larger than the WSM92 dataset available to Bird and Li (1996) (6,000 data points), for which they used $\varepsilon = 0.4$. The larger dataset can be exploited by increasing either the number of discrepancy bins (e.g., using a finer binning for β) or the number of annuli at short range (i.e., $\varepsilon > 0.4$). Based on a series of tests, we chose the latter option. We selected $\varepsilon = 0.6$, which enabled the investigation of short ranges while avoiding high uncertainties for some S_{Hmax} orientations.

We used 150 annuli for the range θ and 30 3°-wide sectors for the discrepancy angle β, resulting in a total of 4,500 bins. Each bin was identified by two indices, $n(\theta)$ and $i(\beta)$, such that the range angle θ lies within the bounds $\theta_{n-1} \leq \theta \leq \theta_n$ and the index i is given by $i = \frac{\beta}{3°} + 1$, rounded down to the nearest integer. The number of data pairs within each bin can be represented by a matrix $C_{i(\beta),n(\theta)}$ of integers.

The probability that a discrepancy β at range θ falls into angular bin i is given by

$$\boldsymbol{D_{i(\beta),n(\theta)} = C_{i(\beta),n(\theta)} / \sum_{j=1}^{30} C_{j,n(\theta)}}. \quad (3)$$

Given a datum r with azimuth α_r, we can define the two-point conditional probability $P(k(\alpha_r)|\alpha_s)$ for any azimuth α_s at any range angle θ determined by the appropriate angular bin k ($0 \leq \alpha < 180$; $k = 1 \ldots 60$):

$$\boldsymbol{P(k(\alpha_r)|\alpha_s) = \frac{1}{2} D_{i(\beta),n(\theta)}}, \quad (4)$$

where the factor of $1/2$ avoids the double counting of pairs (there are two possible azimuths for the same β value for each data pair).

Fig. 3a supports our choice of ε for the investigation of short ranges. The probabilities decrease sharply for the first three annuli with $\varepsilon = 0.6$, whereas smaller values of ε fail to capture this probability variation, resulting in a uniform probability distribution. For example, with $\varepsilon = 0.4$, Annulus 1 contains the upper limit set to 1.76°, whereas for $\varepsilon = 0.6$, this upper limit falls in Annulus 6. Due to the increased number of data points in WSM08 compared to the WSM92 dataset, the finite sample effect for each bin was on the order of 2%, similar to the value found by Bird & Li (1996) in their analysis of the WSM92 dataset.

We divided the WSM08 dataset into five classes according to the quality factor that was assigned to each data record. The probability distributions were of comparable width for the A-, B-, and C-classes (Fig. 3b) and substantially narrower than for the D- and E-classes for all ranges. The D- and E-quality data exhibited a large scatter in the probability distribution at short ranges, indicating a lack of correlation. We therefore discarded the 3,946 data records with D- or E-quality factors and considered only WSM08 data with A-, B-, or C-quality factors in our analysis.

The high probability of finding small discrepancies at short ranges ($\theta \cong 0°$) does not exclude local scatter, as illustrated in Fig. 3c by the non-zero probabilities of high discrepancies in β. These discrepancies are related to the repeatability of the measurements, depth variability, or heterogeneities in the material properties. Following the approach of Barba *et al.* (2010), we estimated the repeatability error at zero distance $\sigma_0 = \sigma(0)$ by interpolating the standard deviation σ versus the range θ using the following equation:

$$\boldsymbol{\sigma(\theta) = a + b\theta + c\theta^{0.5}}. \qquad (5)$$

The error was $\sigma_0 = 4° \pm 1°$ for A-quality data (Fig. 4a), $\sigma_0 = 10.9° \pm 0.6°$ for B-quality data, and $\sigma_0 = 13.2° \pm 0.7°$ for C-quality data. Combining the A-, B-, and C-quality data yields $\sigma_0 = 11.8° \pm 0.5°$ (Fig. 4a).

The inclusion of D-quality data would worsen the results, given the large scatter in the probability distributions for all discrepancies (Figure 3b). The results are affected by both the larger uncertainties for small discrepancies in D-quality data and the larger biases for larger discrepancies. An alternative is weighting the A-, B-, and C-quality data proportionally to the error σ_0 (Eq. 5), which essentially gives a higher weight to A-quality data. Although formally correct (Arnold & Townend, 2007), given the relatively low number of A-quality data compared to B- and C-quality data, the different weighting would have a negligible effect on the results while making the procedure more complex. However, this point may be reconsidered in the future when a greater number of A-quality data are available.

For $\theta < 3°$, the correlation between data pairs is high and the probabilities of large discrepancies are small, whereas for $\theta > 6°$, the discrepancy probabilities do not show any significant trends (Fig. 3c). Following Bird and Li (1996), we define a scalar measure of the correlation as follows:

$$I_{cor}(WSM08) = \frac{\sum_{i=1}^{10} D_i}{\sum_{j=21}^{30} D_j}, \quad (6)$$

i.e., the ratio of D (Eq. 3) for "small" discrepancies ($0 < \beta \leq 30°$) to D with "large" discrepancies ($60° < \beta \leq 90°$). Bird & Li (1996) reported a quasi-exponential falloff of $I_{cor}(WSM92)$ out to a range of 22°, whereas $I_{cor}(WSM08)$ exhibited a quasi-exponential decrease for all ranges (Fig. 4b). To improve the detail at short range, we used the empirical probabilities for $\theta < 3°$ (Annuli 1 to 8) instead of $\theta < 22°$, as adopted by Bird & Li (1996). The choice of the upper value of θ depends on the complexity of the study region. For example, compared to the Pacific Basin in the Tertiary period, the Mediterranean/Tethyan Basin is of similar complexity and has a similar number of subduction zones, yet much shorter along-strike distances. Therefore, the stress fields associated with subduction, mountain ranges and perhaps hanging slabs in the Mediterranean have relatively short length scales compared to those of the Pacific stress fields. Thus, using lower cutoff values than those used in global modelling allows the resolution of these smaller features.

The exponential trend of the probabilities confirms the hypothesis of Bird & Li (1996) that the "correlation horizon" at a range of $\theta = 22°$ is due to uneven sampling of Earth in WSM92. The decreased ringing in $I_{cor}(WSM08)$ with respect to $I_{cor}(WSM92)$ is due to the eightfold increase in the number of unique pairs in WSM08.

2.3. Analytic probabilities and interpolation method

The probability distributions (Fig. 3a) follow an exponential law for all annuli. If few data are considered, the probabilities do not behave exponentially, which explains why this behaviour has not been observed previously. Based on highly successful regressions ($R^2 \geq 0.99$), we parameterised the empirical probabilities of Eq. (4) as follows:

$$\boldsymbol{P^*(k(\alpha_r)|\alpha_s) \equiv P^*(k_r|s) = P_0^* + P_1^* exp(-\theta/\theta_0)}, \quad (7)$$

where P^* denotes the analytic probability and θ_0, P_0^* and P_1^* are constants determined from a nonlinear least-squares fit to the empirical probabilities P (Eq. 4) within the annulus. In this equation, we simplified the notation by using the integer indices r and s in place of the azimuths α_r and α_s. The values of θ_0, P_0^*, and P_1^* for Annuli 1-8 are listed in Table 1.

Let x be a point at which we wish to estimate the stress orientation, and let us select the WSM08 data points within a range of θ_n (Eq. 2). The probability of the azimuth at x falling into bin k given

one datum r is $P^*(k_x|r)$ (Eq. 7). Although the presence of independent data is easily formalised through probability multiplication, clustered data require further analysis. A pair of stress data points r and s form a cluster if

$$P^*(s|r) > \max_{i=r,s} P^*(i|x)\,, \qquad \textbf{(8)}$$

i.e., the two-point conditional probability of r and s is larger than the highest possible conditional probability with respect to the interpolation point x. The opposite guarantees that the data are independent. Note that this definition of independence depends on distance; a pair of data points can both be independent for interpolation points located between the data and form a cluster when they are far away from the interpolation point. After the clusters have been defined, a two-pass procedure is applied. In the first pass, the clustered data are pre-averaged, resulting in a set of fully independent S_{Hmax} orientations. This set consists of pre-averaged data and data points determined to be independent according to Eq. 8. In the second pass, the S_{Hmax} orientation is interpolated to x.

The pre-averaged values of the clustered data are obtained in the first pass using the two-point conditional probability distributions, assuming no azimuthal dependence between the data. For simplicity, we omit the cluster index. The S_{Hmax} orientation of the cluster is assigned to its geographical centre, hereinafter denoted by z, and is determined using the maximum likelihood method. For each trial azimuth, defined by an integer value of k_z ($k_z = 1, \dots, 60$ with 3° bins), we compute the probability as

$$\boldsymbol{P}_{\boldsymbol{N}}^{*}(\boldsymbol{k_z}) = \frac{\prod_{i=1}^{N} \boldsymbol{P}^{*}(\boldsymbol{k_z}|\boldsymbol{i})}{\sum_{j=1}^{60} \prod_{i=1}^{N} \boldsymbol{P}^{*}(\boldsymbol{j_z}|\boldsymbol{i})}, \qquad (\,9\,)$$

where N is the number of stress data forming the cluster. The maximum-likelihood estimate of the S_{Hmax} orientation at the cluster centre z is $\alpha_z = \left(k_z - \frac{1}{2}\right) 3°$, where k_z is the integer that maximises $P_N^*(k_z)$. This operation is performed for each cluster.

In the second pass, the S_{Hmax} orientations are interpolated to x. To identify the now fully independent orientations, we call them "clusters" and label them as c regardless of whether they arose from pre-averaging. For each trial azimuth, defined by an integer value of k_x ($k_x = 1, \dots, 60$ with 3° bins), we calculate the probability as

$$\boldsymbol{P}_{\boldsymbol{N_c}}^{*}(\boldsymbol{k_x}) = \frac{\prod_{c=1}^{N_c} \boldsymbol{P}^{*}(\boldsymbol{k_x}|\boldsymbol{c})}{\sum_{j=1}^{60} \prod_{c=1}^{N_c} \boldsymbol{P}^{*}(\boldsymbol{j_x}|\boldsymbol{c})}, \qquad (\,10\,)$$

where N_c is the number of clusters within range θ_n (Eq. 2). However, the index n is omitted in Eq. (10) for simplicity. The maximum likelihood estimate of the S_{Hmax} orientation at interpolation point x is

$$\alpha_x = \left(k_x - \frac{1}{2}\right) 3°, \quad (11)$$

where k_x is the integer that maximises $P^*_{N_c}(k_x)$ in Eq. (10). The 90% confidence interval $\Delta\alpha$ is determined using the following equation:

$$\int_{\alpha_x - \Delta\alpha}^{\alpha_x + \Delta\alpha} \boldsymbol{p^*_N(\alpha'_x mod 180°)\, d\alpha'_x = 0.90}, \quad (12)$$

where $p^*_N(\alpha'_x mod 180°)$ is the functional form corresponding to the discrete $P^*_N(k_x)$ and "mod" indicates the remainder of the integer division, used to account for the periodicity of α'_x. This procedure allows the uncertainties due to data scattering (shown in Fig. 3 and included in Eq. 10) to propagate into the posterior uncertainties $\Delta\alpha$ (Eq. 12).

We adopt two conditions to ensure a well-defined S_{Hmax} orientation: a) $N_C \geq 3$ within a specified range θ_n and b) $\Delta\alpha \leq 60°$ for the N_C clusters. The upper limit of the 90% confidence interval ($\Delta\alpha \leq 60°$, corresponding to $\sim 2\sigma$ in a normal distribution) accounts for the error associated with C qualities ($1\sigma = 30°$), the most common quality factor in WSM08. The search began with Annulus 1 ($\theta_1 < 0.22°$) and increased stepwise up to Annulus 8 ($\theta_8 < 3°$). We selected the first annulus n (and thus the smallest range) that satisfied both conditions. However, if the conditions were not met by Annulus 8 (the upper limit), then we did not assign an S_{Hmax} orientation to the interpolation point x.

3. Stress interpolation in Europe

We interpolated the WSM08 S_{Hmax} orientations using data-driven analytical weight distributions after pre-averaging the clustered data in the area from 30W to 40E longitude and 25N to 76N latitude. We weighted by distance and discrepancy and adopted thresholds for the number of clusters N_C and the 90% confidence limits $\pm\Delta\alpha$. The threshold values determine the interpolated stress orientations α_x (Eq. 11) and limit the area in which the stress orientations can be recovered (Table 2). We illustrate our results with examples in Europe.

Stress orientations were determined for 57% of the study area. The zones with the smallest $\Delta\alpha$ values are the Apennines, the Dinarides, the Alps, Western Turkey, and the Aegean Sea. We found $\Delta\alpha < 15°$ for 3% of the study area, $\Delta\alpha < 30°$ for 19% of the area, and $\Delta\alpha < 45°$ for 38% of the area (Fig. 5). This fraction of recovered stress orientations is satisfactory and comparable to those obtained in other studies (e.g., Heidbach *et al.*, 2010). The search radius was smaller than the upper limit of Annulus 3 ($\theta_3 < 0.86°$, 96 km) for a large part of continental Europe and the Norwegian Sea (Fig. 6). Conversely, S_{Hmax} was not recovered in the Atlantic Ocean, Northern Africa, or Russia due to the scarcity of data in those locations. The S_{Hmax} orientations were interpolated using

303 $3 \leq N_C \leq 4$ (average number of data $N = 4.87$) for 28% of the study area, $5 \leq N_C \leq 8$ (average
304 $N = 8.89$) for 22% of the study area, $9 \leq N_C \leq 12$ (average $N = 16.05$) for 5% of the study area,
305 and $N_C > 12$ (average $N = 31.42$) for 2% of the study area (Fig. 7). Due to the high density of
306 uniform data, the stress orientations were calculated using large N_C values and short ranges in the
307 Pyrenees, Central Italy, and Romania. Large N_C values and long ranges were used in the Western
308 North Sea, Tyrrenian Sea, Western Alps, and Ionian Sea due to locally scattered WSM08 S_{Hmax}
309 orientations. Our results are provided in both numeric and map form at a resolution of 0.1°× 0.1° as
310 an electronic supplement to this article (Table S1 and Fig. S1).
311 The S_{Hmax} map (Fig. A1, available in the auxiliary material) displays the same main features
312 already described in the literature in relation to the European stress field (Müller *et al.*, 1992; Golke
313 & Coblentz, 1996). The stress pattern in Northwestern Europe (Figure 8a) is dominated by long-
314 wavelength features and follows the NW-SE pattern expected for a stress field produced by plate-
315 scale forces (Müller *et al.*, 1992; Golke & Coblentz, 1996; Müller *et al.*, 1997). Therefore, plate
316 boundary forces are likely the main factor controlling the stress orientation in Northwestern Europe
317 (Goes *et al.*, 2000). Scandinavia exhibits scattered stress orientations (Fig. 8b), likely due to a
318 combination of plate boundary forces, glacial isostatic adjustment, and local heterogeneities
319 (Bungum *et al.*, 2010). However, no clear radial pattern can be observed, indicating that rebound
320 stresses are either spatially limited or of relatively low magnitude. The S_{Hmax} orientations in Iberia
321 display substantial variability (Fig. 8c). The stress field has a complex pattern; first-order
322 compressive stresses, such as the Atlantic ridge push and Eurasia-Africa convergence, interact with
323 and are perturbed by local stress fields, such as the rifting of the Valencia Trough and topographic
324 loading (De Vicente *et al.*, 1996; Andeweg *et al.*, 1999; Liesa and Simon, 2009).
325 In Italy (Fig. 8d), the NNW- SSE S_{Hmax} orientations mark the extension in the Apennines (Boncio
326 & Lavecchia, 2000; Carminati *et al.*, 2001; Barba *et al.*, 2010), whereas the S_{Hmax} in the Adria
327 microplate corresponds with the active Adria-Eurasia compression (Kastelic & Carafa, 2012; Barba
328 et al., 2013). The S_{Hmax} orientations in the Eastern Mediterranean rotate from NNW-SSE to NW-
329 SE in the Marmara Sea and to E-W in the Northern Aegean Sea (Fig. 8e). This pattern follows the
330 lateral extrusion of Anatolia and the N-S directed backarc spreading caused by the rollback of the
331 Hellenic subduction zone (Taymaz *et al.*, 1991; Herget & Heidbach, 2011; Petricca *et al.*, 2013).
332 Short-wavelength features are scattered throughout the map of the interpolated S_{Hmax} orientations.
333 Short-wavelength patterns typically arise from crustal heterogeneities, topographic effects, and
334 sharp variations in the kinematics; we describe a few examples associated with these different
335 causes.

Crustal-scale local stress sources, such as lateral density contrasts, rifting processes, and diapirism, interfere with regional stresses and can result in S_{Hmax} reorientation depending on the stress magnitudes and angular differences. Such a phenomenon occurs in Vrancea and the Southeastern Carpathians (Fig. 8e) and has been extensively studied by Müller *et al.* (2010), who inferred that the high variability in the stress orientations indicates that the stresses generated by local sources are of similar magnitude to the regional stress. In the Central Adriatic (Fig. 8d), the S_{Hmax} orientations also arise from an interplay between the regional stresses, caused by the Adria-Eurasia collision (Kastelic & Carafa, 2012), wrench tectonics, and salt diapirism (Grandic & Markulin, 2000; Geletti *et al.*, 2008; Korbar, 2009). A more extreme case is the easternmost part of the Po Plain, where S_{Hmax} takes on an E-W orientation (Fig. 8d), which is in contrast to the regional N-S compression, as determined from earthquakes and geodesy (Carminati & Vadacca, 2010; Caporali *et al.*, 2011). The smoothed orientations are instead determined using the WSM08 data closest to the interpolation point, which reflect the sedimentary infilling of the Po Plain. The rotation of these stress data with respect to the regional trend can be ascribed to differential sediment compaction, favoured by the presence of anticlines and large variations in the sediment thickness. The shallow E-W orientations of S_{Hmax} due to the tensional, strike-slip stress field at a depth of approximately 1,200 m are perpendicular to the deeper N-S orientations of S_{Hmax} due to the compressive stress field near the main detachment (Carminati *et al.*, 2010). In this specific case, the three closest data points are iso-oriented and represent the sediments, and our algorithm captures the local and shallow tensional stress field induced by the differential sediment compaction. However, applying our algorithm to a different dataset (e.g., the regional moment tensors calculated using the method of Herrmann *et al.*, 2011) yields N-S S_{Hmax} orientations.

In the case of topographically induced stress, S_{Hmax} can align with a mountain chain at the highest elevations and rotate perpendicularly to the chain at the foot of the belt (Assameur & Mareschal, 1995; Carminati *et al.*, 2004). This short-wavelength pattern is evident in the interpolated stress map for the Pyrenean domain (Fig. 8c) and the Eastern and Western Alps (Fig. 8d). However, the pattern is less evident in the Southern Scandes (Fig. 8b) due to the relative scarcity of data there. Parallel trends in S_{Hmax} and the isohypses are typically interpreted as the spreading of topographical crests at high elevation in mountains and as gravitational collapse at mountain bases (Decker *et al.*, 1993; Herraiz *et al.*, 2000; Sue *et al.*, 2007; Pascal & Cloething, 2009; Bungum *et al.*, 2010). In Southern Cyprus, S_{Hmax} follows a N-S orientation (Fig. 8d), supporting the presence of a relatively small collision zone between Cyprus and the Eratosthenes Seamount, which is a faulted block that has been uplifted by 1,500 m. Cyprus and its surroundings are characterised by

NE-SW S_{Hmax} orientations (Fig. 8e) that correspond to the collision between Sinai and Anatolia (Wdowinski *et al.*, 2005).

Another observed short-wavelength feature is the sudden change in tectonic style. Moving from extension to compression implies a rotation of the stress tensor and a consequent rapid reorientation of S_{Hmax}. This phenomenon is observed in the Northern Apennines and Hellenic Arc. As we move from the extension of the Apennines to the compression of the eastern coastline, the S_{Hmax} orientations rotate by 90° within a few tens of kilometres and turn perpendicular to the External Apennines thrust faults (Scrocca, 2006; Basili & Barba, 2007; Carafa & Barba, 2011). Along the Hellenic Arc, similar transitions from extension to compression and subsequent abrupt reorientation of stresses occur in the Central Epirus (Northern Hellenides) and the shallow marine zone between the Ionian Islands and mainland Greece (in the Southern Hellenides) (Papanikolau and Royden, 2007; Jolivet *et al.*, 2009; Papanikolau *et al.*, 2011).

4. Validation

Independent validation is required to understand the degree to which the modelled stress field represents genuine features in Earth's crust. We performed two comparisons: one with synthetic data and one with similar studies available in the literature.

We ran a synthetic checkerboard test to evaluate the significance of short-wavelength stress patterns. The a priori stress flow lines were arranged in 110-km squares, with the stress patterns perpendicular to each other in adjacent squares. S_{Hmax} orientations were assigned to points at 0.2° intervals (Fig. 9). This synthetic data distribution corresponds to a data density of 2.05×10^{-3} data/km^2. To produce three additional synthetic datasets, S_{Hmax} orientations were randomly chosen with assumed data densities of 1.21×10^{-3} data/km^2, 0.81×10^{-3} data/km^2, and 0.37×10^{-3} data/km^2. These values are typical of the WSM08 data densities for much of Europe (Fig. 1), whereas the dimension of the squares and perpendicular S_{Hmax} orientations represent possible stress targets. We applied the interpolation procedure described in the previous section to each of the four datasets (one equispaced and three generated randomly) using the same threshold values ($N_C \geq 3$, $\Delta\alpha < 60°$, and $\theta < 2.94°$) and a spacing of 0.2°. To quantify the agreement between the a priori and recovered checkerboards, we defined a correlation index as the fraction of the recovered S_{Hmax} orientations differing by less than 5° from the initial orientation. As expected, the checkerboard was fully recovered (correlation index equal to one) for the equispaced synthetic dataset (2.05×10^{-3} data/km^2). For the three random datasets, the correlation indices were 0.93 (for 1.21×10^{-3} data/km^2), 0.82 (for 0.81×10^{-3} data/km^2), and 0.70 (for 0.37×10^{-3} data/km^2). The stress patterns were

satisfactorily recovered, both visually (Fig. 10) and according to the correlation index. This test demonstrates that our interpolation procedure can resolve the short-wavelength stress pattern in the parts of Europe with data densities similar to those considered here. In areas with very low data densities (such as Scandinavia and Northern Africa), the S_{Hmax} orientations represent the regional trend and can only be determined using longer ranges (Annulus $n = 6 - 8$, $2.05° < \theta < 2.94°$).

To compare our results with those obtained in similar studies in the literature, we selected the works of Heidbach *et al.* (2010) and Pierdominici & Heidbach (2012). We also applied the Bird & Li (1996) procedure (with pre-averaging and using the Bird & Li (1996) empirical two-point conditional probabilities calculated in WSM92) to WSM08 data. The S_{Hmax} orientations obtained with our method are significantly closer to those of Heidbach *et al.* (2010) than to those obtained by applying the method of Bird & Li (1996) to WSM08 (Fig. 11). This difference arises partly from the algorithm – the range cutoff was $\theta = 22°$ for the global modelling of Bird & Li (1996) versus $\theta = 2.94°$ in our case – and partly from the new set of conditional probabilities based on WSM08. Given the number of data points, the number of unique pairs in WSM08 is eight times larger than that in WSM92. This increase in the number of data pairs permits the investigation of shorter ranges and the resolution of greater spatial detail than in Bird & Li (1996). The S_{Hmax} orientations presented in this work are in good agreement with those from Heidbach *et al.* (2010) for Europe (Fig. 12). The criteria used in the smoothing procedure of Heidbach *et al.* (2010) requires more than five data points to be within a specified search radius and for the standard deviation of these data to be less than 25°. The search radius is initialised at 1,000 km and decreased in 50-km steps until the standard deviation of the $N \geq 5$ S_{Hmax} orientations is less than 25°. Our approach and that presented in Heidbach *et al.* (2010) are both capable of determining the S_{Hmax} orientations for a large part of Europe; our results and theirs overlap by 28%. Within this overlapping region, approximately 10% of the S_{Hmax} orientations (corresponding to 3% of the study area) differ by more than 25°, i.e., more than the standard deviation of Heidbach *et al.* (2010). Approximately 3% of the orientations (corresponding to 1% of the study area) differ by more than 45°, indicating a lack of correlation (Fig. 12), which requires further investigation. Fig. 12 shows the area where the discrepancy in the S_{Hmax} orientations exceeds 25°. Most of these zones (Northeastern Iberia, the Western Alps, the Po Plain, the Northern Apennines, the Southern Tyrrhenian, and Cyprus) are characterised by high data densities (greater than 1.2×10^{-3} data/km^2) and have short-wavelength stress sources and sharply rotating S_{Hmax} orientations, as described in the previous section. Based on these findings, we conclude that our method highlights the presence of short-wavelength stress patterns and sudden S_{Hmax} reorientations ($\theta < 100$ km) that cannot be identified with the minimum search radius of 100 km used in Heidbach *et al.* (2010).

To further validate our method and underline the importance of both pre-averaging the data and investigating short-range stress sources, we compared our results with those of Pierdominici & Heidbach (2012), in which the search radius was decreased from 1,000 km to 100 km in 50-km steps. Their smoothing algorithm requires that more than 10 data points are located in at least two diagonal quadrants of the search circle around the grid point. The two methods display a good overall agreement, with the largest discrepancies in the S_{Hmax} orientations occurring in the Western Alps, Po Plain, Northern Apennines, Central Adriatic, and Southern Tyrrhenian. These zones, characterised by high WSM08 data densities, are the same as those with large discrepancies between our work and that of Heidbach *et al.* (2010) (Fig. 13). We argue that our method performs better in terms of reproducing local patterns and sharp S_{Hmax} rotations, both of which are typical of these high-discrepancy zones.

5. Discussion and conclusions

The method proposed here is appropriate for detecting short-wavelength patterns in S_{Hmax} orientations for large parts of Europe. Our use of analytical probabilities strengthens the contribution of the data close to the interpolation point, where fewer data are available. The data with superior quality factors (A, B, and C) were included, while those with inferior quality factors (D and E) were omitted, which overcomes the difficulties of introducing a weighting scheme into the declustering algorithm.

Müller *et al.* (2003) suggested a search radius between 60 and 200 km for local stress field investigations. We have shown that for data densities greater than 0.8×10^{-3} data/km^2, reliable results can be obtained by pre-averaging the clustered data and choosing a search radius below 60 km (upper limit of Annulus $n = 2$; $\theta_2 < 0.52°$, 58 km). In fact, a few independent data located at short distances tend to highlight local stress sources, whereas a large number of stress data (with a low standard deviation) at greater distances can dominate over the local stress. Increasing the distance increases the likelihood of mixing data affected by different sources of stress. In a few cases, the large number of distant and clustered data could counterbalance the distance weighting. Thus, the orientations of S_{Hmax} could be influenced more by the stress source sampled by the most data than by the local source of stress closest to the interpolation point.

We discuss two examples in which changes in the tectonic regime and rotations in stress orientations occur over short distances and the S_{Hmax} orientations presented here differ from those reported in other studies (Heidbach *et al.*, 2010; Pierdominici & Heidbach, 2012). The first example (Fig. 14) is the transition from the NW-SE-oriented S_{Hmax} field caused by the extension in the

Central Apennines (Bennett *et al.*, 2012) to the NE-SW offshore compression of the Apenninic outer thrust (Boncio & Bracone, 2009; Maesano et *al.*, 2013). When a large search radius is considered (e.g., 100 km), the clustered stress data in the Central Apennines (80% of the data) dominate the stress interpolation along the Adriatic coastline, causing S_{Hmax} to be parallel to the Marche coastline. In our interpolation scheme, 17 WSM08 data are declustered into 12 independent data, or clusters. The search radius for the interpolation point P_m (Fig. 14) is 58 km (corresponding to Annuli 1 and 2). Similar considerations also apply to the second example, concerning the Southern Tyrrhenian (Fig. 15). Moving from west to east, the S_{Hmax} field rotates from NW-SE, related to the Southern Tyrrhenian compression (Giunta *et al.*, 2004), to NE-SW in the Peloritani area, which is undergoing extension. Between these two zones lies the Madonie-Nebrodi area, which is characterised by a NW-SE S_{Hmax} (Sgroi *et al.*, 2011; Palano *et al.*, 2012) that can only be detected with a search radius of less than 60 km. This area is also characterised by a high data density (greater than 0.8×10^{-3} data/km^2), and the search radius for the interpolation point P_s (Fig. 15) is 24 km for the three WSM08 data (which are independent data). In this case, a search radius of 100 km (as in Pierdominci & Heidbach, 2012) captures data primarily related to the Peloritani extension, which is spread over the eastern part of the search area, and results in a different orientation than obtained when using a smaller search radius.

These examples demonstrate that the quantity of data available in WSM08 can be exploited with analytical probabilities by applying a declustering algorithm before interpolating and smoothing the data over a distance less than 60 km from the interpolation point. With future increases in the number of stress data, this approach will help to identify short-wavelength stress patterns and locate shifts in the S_{Hmax} orientations with higher spatial accuracy.

The distance weighting is a key component in the interpolation or smoothing of the data. The various algorithms differ in the weighting function used (see Introduction and Fig. 16 for a comparison). In this work, we used exponentials, which provide high-quality fits to the empirical discrepancy-range relations for the WSM08 data. For the data located near an interpolation point, Heidbach *et al.* (2010) adopted an inverse distance weighting that produces the maximum weight among the methods reviewed in this paper. Bird & Li (1996) employed a more uniform weight at small distances due to the scarcity of data in WSM92. The development of WSM08 (Zang *et al.*, 2012), other available data, and new empirical probabilities will permit further assessment of the quality of the various distance-weighting schemes.

The approach presented here can be used to estimate fault activity through kinematic or dynamic models and to predict the stress orientations of future earthquakes, e.g., for seismic hazard assessment, even where instrumental earthquake recordings are unavailable. Interestingly, several

mountain ranges exhibit 90° rotations of the S_{Hmax} orientation from their crests (which are often in horizontal tension and experience normal faulting) to their foothills (which often undergo thrust faulting). This pattern, seen in the Pyrenees, Alps, Southern Scandes, Hellenic Arc and Apennines, places a strong constraint on the magnitude of the tectonic stresses with respect to the topographic load, a matter that has often debated (e.g., Bird, 1998; Bird et al., 2008). Varying topograpical loads are known to produce stress magnitudes of up to 20-30 MPa, which significantly influences the stress orientations. This influence occurs not only in continental Europe (Golke & Coblentz, 1996), where tectonic stresses are very small, but also in the Alpine-Dinaric belt and Pannonian Basin, where 2-km changes in elevation generate tensional stresses ranging from 6 to 22 MPa in the mountain belt and compressional stresses ranging from 3 to 12 MPa in the basin (Bada et al., 2001). Tectonic stresses are often estimated to be high at plate boundaries due to ridge push or sinking slabs (80-120 MPa; Whittaker et al., 1992), but these stresses are expected to produce observable shear heating (e.g., Molnar and England, 1990). However, the influence of these stresses within continents remains controversial. In fact, stresses on major faults have been found to be smaller than 30 MPa (e.g., Mount and Suppe, 1987; Zoback et al., 1987), and basal tractions acting across continents have been estimated to produce changes of up to 20 MPa in compressive stresses (e.g., Bird, 1998; Gosh et al., 2008). The 90° rotation of the S_{Hmax} suggests that, at least in the mountain ranges where these rotations are observed, the magnitude of tectonic and topographic stress must be comparable, thus supporting the hypothesis that tectonic stresses can be characterized by relatively low magnitudes of 20-30 MPa. As an indirect consequence, this finding supports the idea that topographic stress can cause an inversion, at a certain depth, of the expected pattern of differential stress, allowing for the initiation of ruptures on low-angle thrust faults at shallow depths to propagate downward (Carminati et al., 2004).

The derived S_{Hmax} orientations describe the present-day stress field in Europe. The proposed approach produced acceptable uncertainties for nearly half of Europe. The modified Bird & Li (1996) algorithm facilitates the identification of third-order features, such as topography effects and crustal-scale density heterogeneities. The stress orientations modelled in this work are generally compatible with those of previous studies. However, for areas with data densities greater than 0.8×10^{-3} data/km^2, our algorithm outperforms the existing methods in identifying short-wavelength stress sources.

Acknowledgements

We thank the associate editor Saskia Goes, Peter Bird, and John Townend for their thorough reviews. We thank D. Coblentz for his valuable comments on an early version of the manuscript, S. Pierdominici for kindly supplying the results of her work, O. Heidbach for suggesting that we perform synthetic tests, and again P. Bird for the NeoKinema.f90 code, which helped us to design our work. This work was supported by the DPC-INGV 2008-2010 S1 project, the EU-FP7 project "Seismic Hazard Harmonization in Europe" (SHARE; Grant agreement no. 226967), and project MIUR-FIRB "Abruzzo" (code: RBAP10ZC8K_003). Some figures were created using Generic Mapping Tools (Wessel & Smith, 1998).

References

Amante, C. & Eakins, B. W., 2009. ETOPO1 1 Arc-Minute Global Relief Model: Procedures, Data Sources and Analysis. NOAA Technical Memorandum NESDIS NGDC-24, 19 pp, March 2009.

Andeweg, B., De Vicente, G., Cloetingh, S., Giner, J. & Muñoz Martin, A., 1999. Local stress fields and intraplate deformation of Iberia: variations in spatial and temporal interplay of regional stress sources, Tectonophysics, 305, 153–164

Arnold, R. & Townend, J., 2009. A Bayesian approach to estimating tectonic stress from seismological data. Geophys. J. Int., 170, 1336–1356, doi: 10.1111/j.1365-246X.2007.03485.x

Assameur, D.M. & Mareschal, J.-C., 1995. Stress induced by topography and crustal density heterogeneities: implication for the seismicity of southeastern Canada, Tectonophysics, 241 (3–4), 179–192.

Bada, G., Horvath, F., Cloetingh, S. & Coblentz, D.D., 2001. Role of topography-induced gravitational stresses in basin inversion: the case study of the Pannonian basin, Tectonics, 20, 343-363.

Barba, S., Carafa, M.M.C., Mariucci, M. T., Montone, P. & Pierdominici, S., 2010. Present-day stress field modelling of southern Italy constraining by stress and GPS data, Tectonophysics, 482 (1-4), 193-204.

Barba, S., Finocchio, D., Sikdar, E. & Burrato, P., 2013. Modeling the interseismic deformation of a thrust system: seismogenic potential of the Southern Alps, Terra Nova, in press, doi: 10.1111/ter.12026

Basili, R. & Barba, S., 2007. Migration and shortening rates in the Northern Apennines, Italy: implications for seismic hazard, Terra Nova, 19 (6), 462-468.

563 Bennett, R. A., Serpelloni, E., Hreinsdóttir, S., Brandon, M. T., Buble, G., Basic,T., Casale,
564 G., Cavaliere, A., Anzidei, M., Marjonovic, M., Minelli, G., Molli, G. & Montanari, A., 2012. Syn-
565 convergent extension observed using the RETREAT GPS network, northern Apennines, Italy, J.
566 Geophys. Res., 117, B04408, doi:10.1029/2011JB008744.
567 Bird, P. & Li, Y., 1996. Interpolation of principal stress directions by nonparametric
568 statistics: Global maps with confidence limits, J. Geophys. Res., 101(B3), 5,435 – 5,443.
569 Bird, P., 1998. Testing hypotheses on plate-driving mechanisms with global lithosphere
570 models including topography, thermal structure, and faults, J. Geophys. Res., 103 (B5), 10,115-
571 10,129.
572 Bird, P., Liu, Z. & Rucker, W.K., 2008. Stresses that drive the plates from below:
573 Definitions, computational path, model optimization, and error analysis, J. Geophys. Res., 113,
574 B11406, 1-32.
575 Boncio, P. & Lavecchia, G., 2000. A structural model for active extension in central Italy,
576 Journal of Geodynamics, 29, 233–244.
577 Boncio, P. & Bracone, V., 2009. Active stress from earthquake focal mechanisms along
578 the Padan-Adriatic side of the Northern Apennines (Italy), with considerations on stress magnitudes
579 and pore-fluid pressures, Tectonophysics, 476 (1-2), 180-194, doi: 10.1016/j.tecto.2008.09.018.
580 Bungum, H., Olesen, O., Pascal, P., Gibbons, S., Lindholm, C., & Vestøl, O., 2010. To what
581 extent is the present day seismicity in Norway driven by post-glacial rebound?, J. Geol. Soc.,
582 London, 167, 373–384, doi:10.1144/0016-76492009-009.
583 Caporali, A., Barba, S., Carafa, M.M.C., Devoti, R., Pietrantonio, G. & Riguzzi, F., 2011.
584 Static stress drop as determined from geodetic strain rates and statistical seismicity, J. Geophys.
585 Res., 116, B02410.
586 Carafa, M.M.C. & Barba, S., 2011. Determining rheology from deformation data: The case
587 of central Italy, Tectonics, 30, TC2003.
588 Carminati, E., Doglioni, C. & Barba, S., 2004. Reverse migration of seismicity along thrusts
589 and normal faults, Earth-Sci. Rev., 65 (3-4), 195-222, doi:10.1016/S0012-8252(03)00083-7.
590 Carminati, E., & Vadacca, L., 2010. Two- and three-dimensional numerical simulations of
591 the stress field at the thrust-front of the Northern Apennines, Italy, J. Geophys. Res., 115, B12425.
592 Carminati, E., Scrocca, D. & Doglioni, C., 2010. Compaction-induced stress variations with
593 depth in an active anticline: Northern Apennines, Italy, J. Geophys. Res., 115, B02401.
594 Carminati, E., Toniolo Augier, F. & Barba, S., 2001. Dynamic modeling of stress
595 accumulation in central Italy: Role of structural heterogeneities and rheology, Geophys. J. Int., 144,
596 373 – 390.

Coblentz, D.D. & Richardson, R.M., 1995. Statistical Trends in the Intraplate Stress Field, J. Geophys. Res., 100 (20), 245-255.

Decker, K., Meschede, M. & Ring, U., 1993. Fault slip analysis along the northern margin of the Eastern Alps (Mollasse, Helvethic nappes, North- and South-Penninic flysch and the Northern Calcareous Alps), Tectonophysics, 223, 291–312.

De Vicente, G., Giner, J.L., Munoz Martin, A., Gonzalez-Casado, J.M. & Lindo, R., 1996. Determination of present-day stress tensor and neotectonic interval in the Spanish Central System and Madrid Basin, central Spain, Tectonophysics, 266, 405–424.

Geletti, R., Del Ben, A., Busetti, M., Ramella, R. & Volpi V., 2008. Gas seeps linked to salt structures in the Central Adriatic Sea, Basin Res., 20, 473–487.

Ghosh, A., Holt, W.E., Wen, L., Haines, A.J. & Flesch, L.M., 2008. Joint modeling of lithosphere and mantle dynamics elucidating lithosphere-mantle coupling. Geophysical Research Letters, 35, L16309, 1-5.

Grandić, S. & Markulin, Ž., 2000. Triassic synrift euxinic basins as a factor of exploration risk in the Croatian offshore area, Proceedings of International Symposium of Petroleum Geology, April 22–24, 1999, Nafta (Zagreb, Croatia), 51(spec. issue), 41–50.

Goes, S., Loohuis, J.J.P., Wortel, M.J.R. & Govers R., 2000. The effect of plate stresses and shallow mantle temperatures on tectonics of northwestern Europe, Global and Planetary Change, 27, 23–39.

Gölke, M. & Coblentz, D., 1996. Origins of the European regional stress field, Tectonophysics, 266, 11–24.

Ghisetti, F.C. & Sibson, R.H., 2012. Compressional reactivation of E–W inherited normal faults in the area of the 2010–2011 Canterbury earthquake sequence, New Zealand Journal of Geology and Geophysics, 55:3, 177-184. DOI:10.1080/00288306.2012.674048

Giunta, G., Luzio, D., Tondi, E., De Luca, L., Giorgianni, A., D'Anna, G., Renda, P., Cello, G., Nigro, F. & Vitale, M., 2004. The Palermo (Sicily) seismic cluster of September 2002, in the seismotectonic framework of the Tyrrhenian Sea–Sicily border area, Annals of Geophysics, 47 (6), 1755–1770.

Hansen, K. M. & Mount, V. S., 1990. Smoothing and extrapolation of crustal stress orientation measurements, J. Geophys. Res., 95(B2), 1155–1165, doi:10.1029/JB095iB02p01155.

Hardebeck, J. L. & Michael, A. J., 2006. Damped regional-scale stress inversions: Methodology and examples for southern California and the Coalinga aftershock sequence, J. Geophys. Res., 111, B11310, doi:10.1029/2005JB004144.

630 Heidbach, O., Tingay, M., Barth, A., Reinecker, J., Kurfeß, D. & Müller, B., 2008. The
631 World Stress Map database release 2008. Available at
632 http://dx.doi.org/10.1594/GFZ.WSM.Rel2008.
633 Heidbach, O., Tingay, M., Barth, A., Reinecker, J., Kurfeß, D. & Müller, B., 2010. Global
634 crustal stress pattern based on the World Stress Map database release 2008, Tectonophysics, 482, 3-
635 15.
636 Hergert, T. & Heidbach, O., 2011. Geomechanical model of the Marmara Sea region - II. 3-
637 D contemporary background stress field, Geophys. J. Int., 185 (3),1090-1102.
638 Herraiz, M., De Vicente, G., Lindo, R., Giner, J.L., Simón, J.L., González-Casado, J.M.,
639 Vadillo, O., Rodríguez-Pascua, M.A., Cicúendez, J.I., Casas, A., Cabañas, L., Rincón, P., Cortés,
640 A.L., Ramírez, M. & Lucini, M., 2000. The recent (upper Miocene to Quaternary) and present
641 tectonic stress distributions in the Iberian Peninsula, Tectonics, 19 (4), 762–786.
642 Herrmann, R.B., Malagnini, L., Munafo, I., 2011. Regional moment tensors of the 2009
643 L'Aquila earthquake sequence, Bull. Seism. Soc. Am., 101, 975-993.
644 Kastelic, V. & Carafa, M.M.C., 2012. Fault slip rates for the active External Dinarides
645 thrust-and-fold belt, Tectonics, 31, TC3019.
646 Korbar, T., 2009. Orogenic evolution of the External Dinarides in the NE Adriatic region: A
647 model constrained by tectonostratigraphy of Upper Cretaceous to Paleogene carbonates, Earth Sci.
648 Rev., 96 (4), 296–312.
649 Jolivet, L., Faccenna, C. & Piromallo, C., 2009. From mantle to crust: Stretching the
650 Mediterranean, Earth Planet. Sci. Lett., 285, 198–209, doi:10.1016/j.epsl.2009.06.017.
651 Lee, J. C. & Angelier, J., 1994. Paleostress trajectory maps based on the results of local
652 determinations: the ‘‘Lissage’’ program, Comput. Geosci., 20, 161– 191.
653 Liesa, C.L. & Simón, J.L., 2009. Evolution of intraplate stress fields under multiple remote
654 compressions: The case of the Iberian Chain (NE Spain), Tectonophysics, 474 (1-2): 144-159.
655 Lund, B. & Townend, J., 2007. Calculating horizontal stress orientations with full or partial
656 knowledge of the tectonic stress tensor, Geophys. J. Int., 170 (3), 1328–1335, doi:10.1111/j.1365-
657 246X.2007.03468.x.
658 Maesano, F. E., Toscani, G., Burrato, P., Mirabella, F., D'Ambrogi, C. & Basili, R., 2013.
659 Deriving thrust fault slip rates from geological modeling: Examples from the Marche coastal and
660 offshore contraction belt, Northern Apennines, Italy, Mar. Petrol. Geol. (in press),
661 doi:10.1016/j.marpetgeo.2012.10.008.
662 Mardia, K.V., 1972. Statistics of Directional Data:Probability and Mathematical Statistics,
663 Academic Press, London. 357 pp.

664 Molnar, P. & England, P., 1990. Temperatures, heat flux, and frictional stress near major
665 thrust faults. Journal of Geophysical Research, 95, B4, 4833-4856.
666 Mount, V.S. & Suppe, J., 1987. State of stress near the San Andreas fault: implications for
667 wrench tectonics, Geology, 15, 1143-1146
668 Müller, B., Heidbach, O., Negut, M., Sperner, B., & Buchmann, T., 2010. Attached or not
669 attached - evidence from crustal stress observations for a weak coupling of the Vrancea slab in
670 Romania, Tectonophysics, 482 (1-4), 139-149.
671 Müller, B., Wehrle, V., Hettel, S., Sperner, B. & Fuchs, K., 2003. A new method for
672 smoothing orientated data and its application to stress data, in Fracture and In-Situ Stress
673 Characterization of Hydrocarbon Reservoirs, edited by M. S. Ameen, Geol. Soc. Lond. Spec. Publ.,
674 209, 107 – 126.
675 Müller, B., Wehrle, V., Zeyen, H.J. & Fuchs, K., 1997. Short-scale variations of tectonic
676 regimes in the western European stress province north of the Alps and Pyrenees, Tectonophysics,
677 275, 199–219.
678 Müller, B., Zoback, M.L., Fuchs, K., Mastin, L., Gregersen, S., Pavoni, N., Stephansson, O.
679 & Ljunggren, C., 1992. Regional patterns of tectonic stress in Europe, J. Geophys. Res. 97, 11783–
680 11803.
681 Palano, M., Ferranti, L., Monaco, C., Mattia, M., Aloisi, M., Bruno, V., Cannavò, F. &
682 Siligato, G., 2012. GPS velocity and strain fields in Sicily and southern Calabria, Italy: Updated
683 geodetic constraints on tectonic block interaction in the central Mediterranean, J. Geophys. Res.,
684 117, B07401, doi:10.1029/2012JB009254
685 Papanikolaou, D., & L. Royden (2007), Disruption of the Hellenic arc: Late Miocene
686 extensional detachment faults and steep Pliocene-Quaternary normal faults—Or what happened at
687 Corinth?,Tectonics, 26, TC5003, doi:10.1029/2006TC002007.
688 Papanikolaou, D., Royden, L. & Vassilakis, E., 2011. Neotectonic and active diverging rates
689 of extension in the northern and southern Hellenides across the central Hellenic shear zone, in:
690 INQUA-IGCP 567 Proceedings Vol.2, Edited by INQUA-TERPRO Focus Area on
691 Paleoseismology and Active Tectonics & IGCP-567 Earthquake Archaeology, Printed in Greece,
692 ISBN 978-960-466-093-3.
693 Pascal, C. & Cloetingh, S.A.P.L., 2009. Gravitational potential stresses and stress field of
694 passive continental margins: Insights from the south Norway shelf, Earth Planet. Sci. Lett., 277,
695 464-473.

696 Petricca, P., Carafa, M. M. C., Barba, S. & Carminati, E., 2013. Local, regional, and plate
697 scale sources for the stress field in the Adriatic and Periadriatic region, Mar. Petrol. Geol., in press,
698 10.1016/j.marpetgeo.2012.08.005.
699 Pierdominici, S. & Heidbach, O., 2012. Stress field of Italy - Mean stress orientation at
700 different depths and wave-length of the stress pattern, Tectonophysics, 532-535, 301-311.
701 Rebai, S., Herve, P. & Taboada, A., 1992. Modern tectonic stress field in the Mediterranean
702 region: Evidence for variation in stress directions at different scales, Geophys. J. Int., 110, 106-140.
703 Scrocca, D., 2006. Thrust front segmentation induced by differential slab retreat in the
704 Apennines (Italy), Terra Nova, 18, 154–161.
705 Sgroi, T., de Nardis, R. & Lavecchia, G., 2012. Crustal structure and seismotectonics of
706 central Sicily (southern Italy): new constraints from instrumental seismicity, Geophysical Journal
707 International, 189 (3), 1237–1252.
708 Sibson, R., Ghisetti, F. & Ristau, J., 2011. Stress control of an evolving strike-slip fault
709 system during the 2010–2011 Canterbury, New Zealand, earthquake sequence. Seismological
710 Research Letters, 82, 824–832. DOI:10.1785/gssrl.82.6.824
711 Syracuse, E.M., Holt, R.A., Savage, M.K., Johnson, J.H., Thurber, C.H., Unglert, K., Allan,
712 K.N., Karaliyadda, S. & Henderson, M., 2012. Temporal and spatial evolution of hypocentres and
713 anisotropy from the Darfield aftershock sequence: implications for fault geometry and age, New
714 Zealand Journal of Geology and Geophysics, 55:3, 287-293. DOI:10.1080/00288306.2012.690766
715 Sue, C., Delacou, B., Champagnac, J.D., Allanic, C., Tricart, P. & Burkhard, M., 2007.
716 Extensional neotectonics around the bend of the Western/Central Alps: an overview, Int. J. Earth
717 Sci., 96, 1101-1129.
718 Taymaz, T., Jackson, J. & McKenzie, D., 1991. Active tectonics of the north and central
719 Aegean Sea, Geophys. J. Int., 106, 433-490.
720 Wessel, P. & Smith, W.H.F., 1998. New, improved version of the Generic Mapping Tools
721 released, Eos Trans. AGU, 79, 579.
722 Wdowinski, S., Ben-Avraham, Z., Arvidsson, R. & Ekstroem, G., 2006. Seismotectonics of
723 the Cyprian Arc, Geophys. J. Int., 164, 176-181.
724 Whittaker, A., Bott, M.H.P. & Waghorn, G.D., 1992. Stresses and plate boundary forces
725 associated with subduction plate margins. Journal of Geophysical Research, 97, B8, 11,933-11,944.
726 Zang, A., Stephansson, O., Heidbach, O., & Janouschkowetz, S., 2012. World Stress Map
727 Database as a Resource for Rock Mechanics and Rock Engineering, Geotechnical and geological
728 Engineering, 30 (3), 625-646.

729 Zoback, M.D., Zoback, M. L., Mount, V. S., Suppe, J., Eaton, J.P., Healy, J. H.,
730 Oppenheimer, D., Reasenberg, P., Jones, L., Raleigh, C. B., Wong, I. G., Scotti, O. & Wentworth,
731 C., 1987. New evidence on the state of stress of the San Andreas fault system, Science, 238, 1105-
732 1111.
733 Zoback, M.L., 1992. First and second order patterns of stress in the lithosphere: the World
734 Stress Map Project, J. Geophys. Res., 97(B8), 11703-1172.

Table Captions

Table 1. Regression parameters and related standard error of Eq. (7) for Annuli 1 to 8. P_0^*, P_1^*, and θ_0: coefficients of Eq. (7) considering the associated standard errors. RMS: root mean square between empirical and analytical probabilities. R^2: coefficient of determination, which measures the goodness of the regression fit.

Table 2. Percentage of the area in which the stress orientations can be recovered for various threshold values of $\Delta\alpha$ and N_C, with the maximum search radius set to the upper limit of Annulus 8 ($\theta_8 < 2.94°$; 327 km). The total extent of the study area is 2.71×10^9 km^2.

Figure Captions

Figure 1. WSM08 data density in Europe. Densities were computed for 0.5°×0.5° cells, from 25N to 76N latitude and 30W to 40E longitude. Cells with no data entries are not coloured.

Figure 2. Cartographic description of the discrepancy angle β. For each pair of stress data points, r and s, we define the great circle (green line) between r and s for an oblique Mercator projection. The discrepancy is the angle between the two S_{Hmax} orientations as expressed in Eq. (1). The S_{Hmax} orientations of r and s are shown in black, and the S_{Hmax} orientation of s, translated onto r, is shown in grey.

Figure 3. Probability distributions as a function of discrepancy and range. (a) Analytical (lines) and empirical (symbols) probabilities for Annuli (An) 1-3 (A-C quality factors); (b) empirical probabilities for Annulus 1 for A-E quality factors; (c) empirical probabilities for various discrepancy intervals. The lines connect the empirical values in (b) and (c).

Figure 4. (a) Standard deviation versus range (symbols) and analytical representation of Eq. (5) (SV: lines, with confidence limits); (b) the ratio of D (Eq. 3) for "small" discrepancies ($0 < \beta \leq 30°$) to "large" discrepancies ($60° < \beta \leq 90°$) versus range.

Figure 5. Colour-coded map of the 90% confidence limits ($\pm\Delta\alpha$).

Figure 6. Minimum search radius for which $\Delta\alpha < 60°$ and $N_C \geq 3$. The upper bound is set to $\theta = 2.94°$.

Figure 7. Number of clusters N_C used to interpolate S_{Hmax}.

Figure 8. S_{Hmax} orientations in Europe. (a) Northwestern Europe; (b) Scandinavia; (c) Iberia; (d) Italy; (e) Southeastern Europe. Thick bars: WSM08 data; thin black bars: interpolated S_{Hmax} (this work). Inset: colour-coded map of the 90% confidence limits ($\pm\Delta\alpha$).

Figure 9. Input synthetic checkerboard stress orientations.

Figure 10. Results of the checkerboard test. From left to right: (1's) S_{Hmax} orientations randomly selected from the checkerboard shown in Figure 9; (2's) interpolated stress field with the same threshold values used to calculate the S_{Hmax} orientations in Europe ($N_C \geq 3, \Delta\alpha < 60°, \theta < 2.94°$); (3's) minimum search radius. From top to down: (a's) Data density of 1.21×10^{-3} data/km^2; (b's) data density of 0.81×10^{-3} data/km^2; (c's) data density of 0.37×10^{-3} data/km^2.

Figure 11. (a) Discrepancies between the S_{Hmax} stress orientations presented in this work and those obtained using the WSM08 and the probability distributions of Bird and Li (1996). The values are calculated on the Heidbach *et al.* (2010) grid. (b) Frequency distributions of the discrepancies (grey histogram: relative frequency; black line: cumulative frequency).

Figure 12. (a) Discrepancies between the S_{Hmax} orientations presented in this work and those of Heidbach *et al.* (2010). The values are calculated on the Heidbach *et al.* (2010) grid. (b) Frequency distributions of the discrepancies (grey histogram: relative frequency; black line: cumulative frequency).

Figure 13. Interpolated S_{Hmax} orientations in Italy, calculated on the Pierdominici & Heidbach (2012) grid. The colours indicate the discrepancies between the S_{Hmax} orientations obtained using the algorithm presented here and the orientations of Pierdominici and Heidbach (2012). The rectangles indicate the areas shown in Figures 14 and 15.

Figure 14. Comparison of the S_{Hmax} orientation obtained using our algorithm with that obtained by Pierdominici & Heidbach (2012) for the external Apennines. See Fig. 13 for the location of the area. Thick black bar (PH2012): smoothed S_{Hmax} orientation calculated by Pierdominici & Heidbach (2012) with a search radius of 100 km; thick grey bar: interpolated S_{Hmax} orientation obtained in the present work ($N_C = 12$; search radius $\theta = 0.52°$, 58 km); P_m: interpolation point. The background colours indicate the discrepancies between the S_{Hmax} orientations obtained using the algorithm presented here and those of Pierdominici and Heidbach (2012). The multicolour lines denote the S_{Hmax} orientations for different kinematic regimes (WSM08; Heidbach *et al.*, 2008). Tectonic regime identifiers: NF, normal fault; NS, normal-oblique; SS, strike-slip; TS, thrust-oblique; TF, thrust; U, unknown tectonic regime.

Figure 15. Comparison of the S_{Hmax} orientation obtained using our algorithm ($N_C = 13$; search radius $\theta = 0.52°$, 58 km; P_s: interpolation point) with that obtained by Pierdominici & Heidbach (2012) for Northern Sicily. See Fig. 13 for the location of the area and the caption of Fig.14 for further explanations.

Figure 16. Normalised distance weight of different algorithms for points at distances between 20 and 340 km with 20-km steps.

Figure A1. S_{Hmax} orientations in Europe with confidence limits. Red bars: interpolated orientations (this work); black bars: confidence limits (this work). Relief model from ETOPO1 (Amante and Eakins, 2009).

Supplementary files

The following files and figure are for the online download.

Table_S1.csv: contains the interpolated stress orientations in Europe (330W-40E;25N-76N)
Column "ANN" contains the searching radius (expressed as Annulus number). To convert in degrees, use eq. (2).
Column "Lat" contains the latitude of the interpolation point (degrees).
Column "Lon" contains the longitude of the interpolation point (degrees).
Column "AZI" contains the azimuth of the maximum horizontal compressive stress orientations (degrees).
Column "C90" contains the 90% confidence interval for the maximum horizontal compressive stress orientations (degrees).
Column "N" contains the number data (from World Stress Map release 2008) falling into the search circle.
Column "Nc" contains the number of clusters.

Table_S1.csv.gz: same as Table_A1.csv, in compressed (gzip) format.

Figure_S1.pdf: SHmax orientations in Europe with confidence limits.
Red bars: interpolated orientations (this work). Black bars: confidence limits (this work). Relief model from ETOPO1 (Amante and Eakins, 2009).

Table_S1_Carafa_Barba.kmz contains Table S1 in Google Earth format. In order for the kmz to work properly, the file icon.png must be located in the same directory of the kmz.

Important notes. The size of the kmz can slow down the computer and let Google Earth lock.
We recommend proceeding as follows:
1) verify that the kmz and the icon.png are located in the same directory

2) launch Google Earth (do not click open the kmz at this stage)

3) zoom in the area of interest

4) open the kmz (File...Open, or click open the kmz)

First published online: February 19, 2013

http://gji.oxfordjournals.org/content/early/2013/02/19/gji.ggt024.abstract

Note that the online version currently has two versions of the supplementary material, one (the wrong version) has the DC1 in the directory name, whereas the correct version has DC2 in the directory name. The full link to the accompanying material is http://gji.oxfordjournals.org/content/suppl/2013/02/21/ggt024.DC2/ggt024-supplementary_files.zip

Comments to michele.carafa@ingv.it and salvatore.barba@ingv.it

Thanks to Gabriele Tarabusi for helping with the kml conversion.

Table 1

Table 1. Regression parameters and related standard error of Eq. (7) for Annuli 1 to 8. P_0^*, P_1^*, and θ_0: coefficients of Eq. (7) considering the associated standard errors. RMS: root mean square between empirical and analytical probabilities. R^2: coefficient of determination, which measures the goodness of the regression fit.

Annulus	$P_0^* \cdot 10^{-3}$	St. error $P_0^* \cdot 10^{-3}$	$P_1^* \cdot 10^{-3}$	St. error $P_1^* \cdot 10^{-3}$	θ_0 (degrees)	St. error θ_0 (deg)	RMS (10^{-3})	R^2
1	4.6	0.4	204	1	12.7	0.1	1.3	0.999
2	7.6	0.3	140.5	0.7	16.6	0.2	0.8	0.999
3	12.7	0.6	102	1	18.4	0.5	1.6	0.996
4	14.9	0.8	81	1	20.7	0.9	1.8	0.993
5	14.2	0.9	70	1	25	1	1.7	0.991
6	14	1	65	1	28	2	1.8	0.989
7	13.8	0.9	57.1	0.8	33	2	1.1	0.995
8	14.8	0.8	51.4	0.7	35	2	0.8	0.996

Table 2

Table 2. Percentage of the area in which the stress orientations can be recovered for various threshold values of $\Delta\alpha$ and N_C, with the maximum search radius set to the upper limit of Annulus 8 ($\theta_8 < 2.94°$; 327 km). The total extent of the study area is 2.71×10^9 km^2.

Minimum number of clusters (N_C)	Maximum value of 90% confidence interval $\Delta\alpha$			
	20°	40°	60°	80°
1	18%	44%	59%	75%
3	18%	44%	57%	63%
5	18%	43%	52%	56%
7	18%	40%	46%	49%

Figure 1

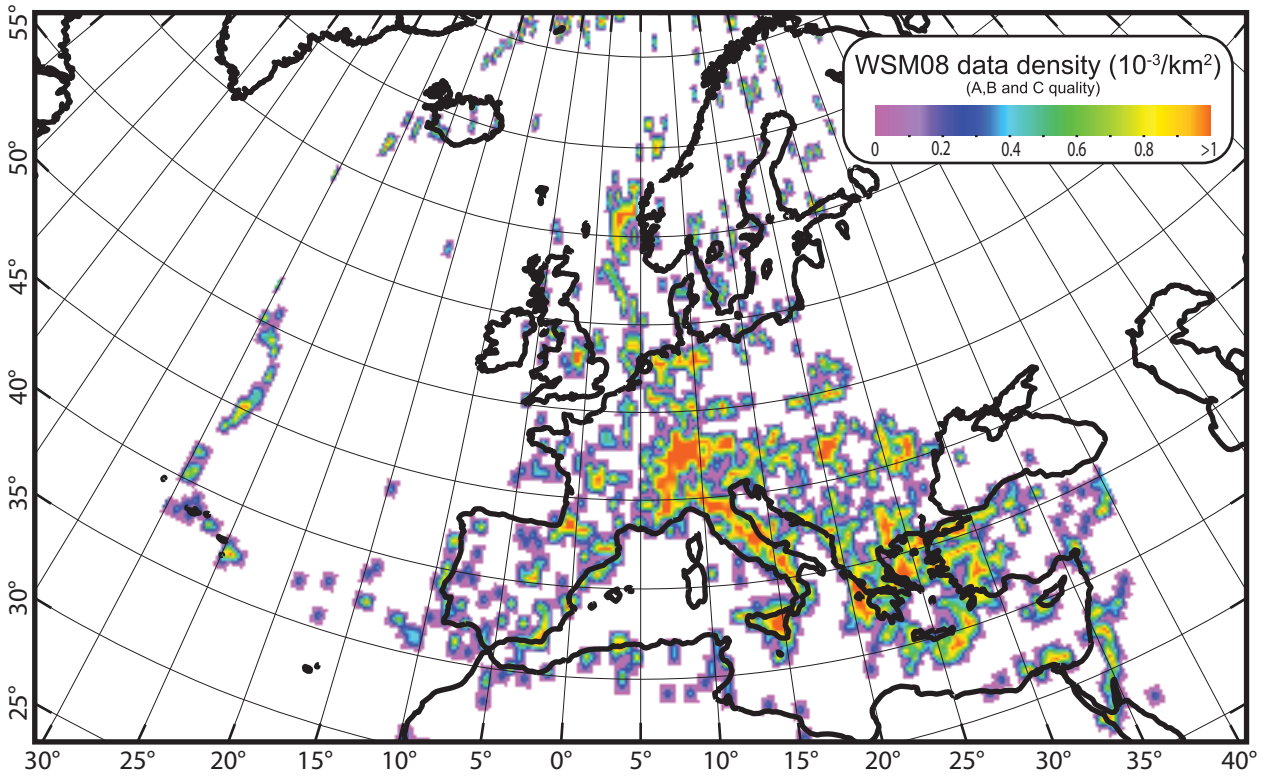
WSM08 data density (10-3/km2)
(A,B and C quality)
0
0.2
0.4
0.6
0.8
>1
55°
50°
45°
40°
35°
30°
25°
30°
25°
20°
15°
10°
5°
0°
5°
10°
15°
20°
25°
30°
35°
40°

Figure 2

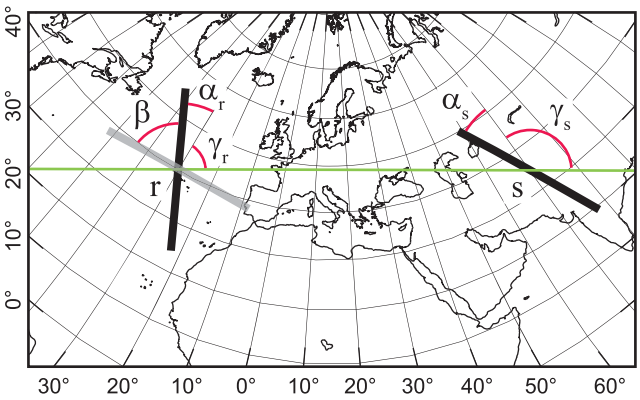
40°
30°
20°
10°
0°
30°
20°
10°
0°
10°
20°
30°
40°
50°
60°
α_r
β
γ_r
r
α_s
ζ
γ_s
s

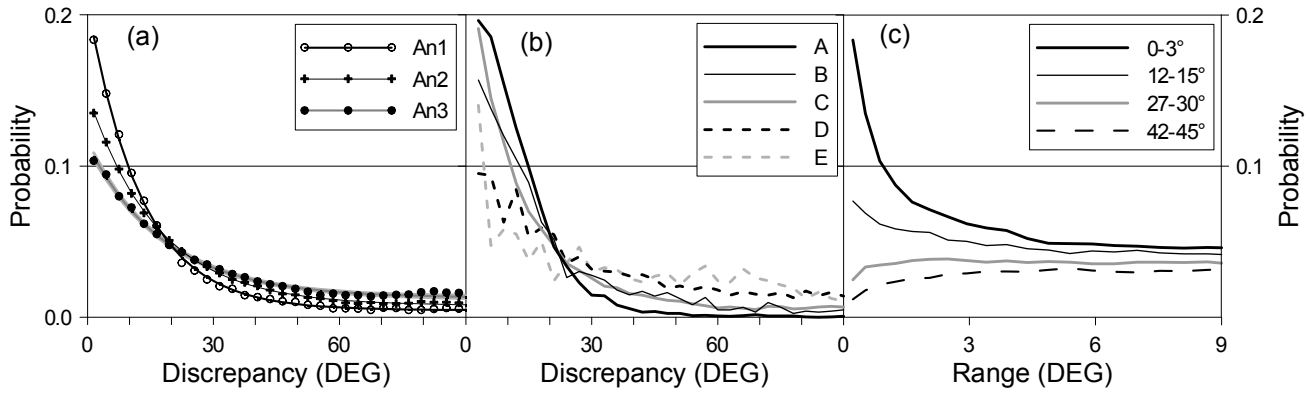
(a)
(b)
(c)
An1
An2
An3
A
B
C
D
E
0-3°
12-15°
27-30°
42-45°
Probability
Discrepancy (DEG)
Discrepancy (DEG)
Range (DEG)
0.0
0.1
0.2
0
30
60
3
6
9

Figure 3

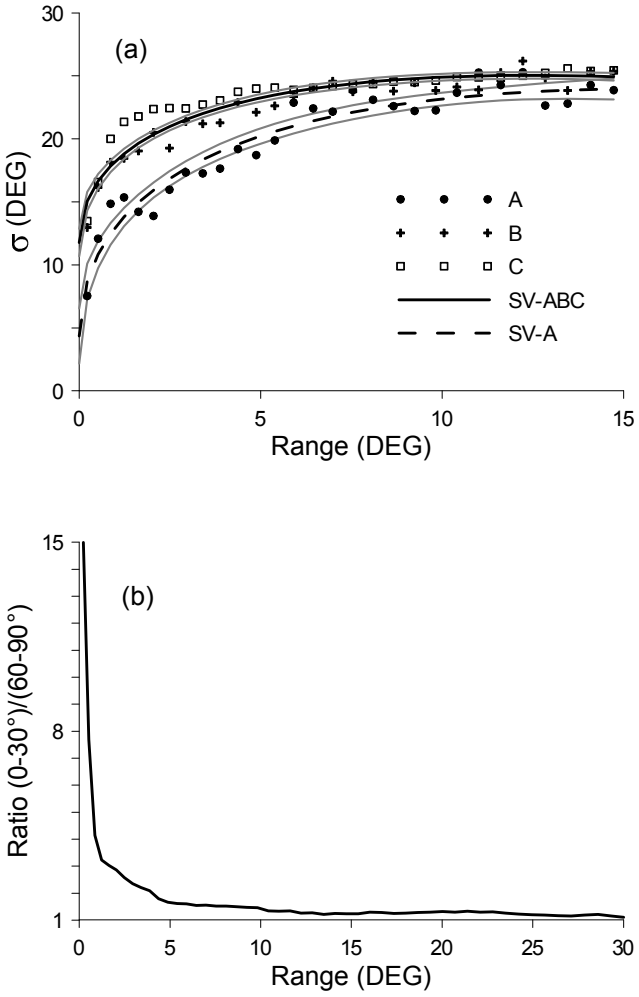

Figure 4

Figure 5

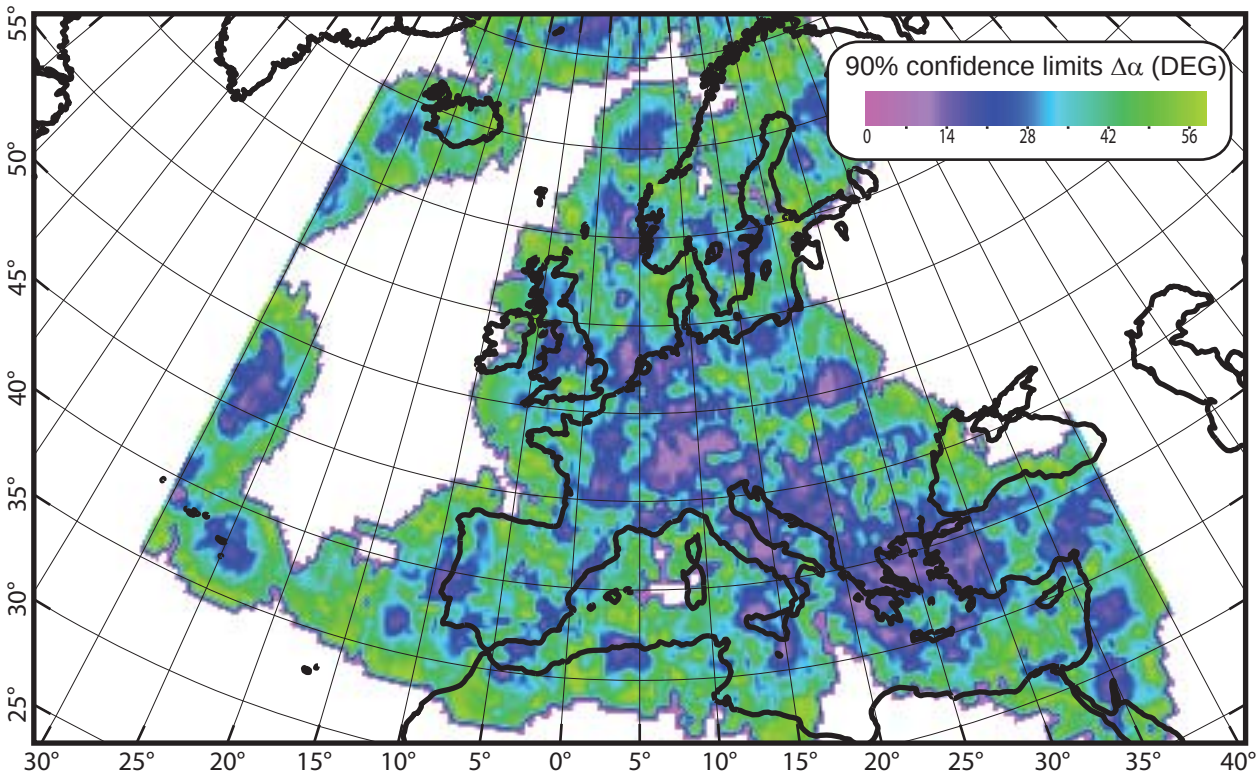
90% confidence limits Δα (DEG)
0
14
28
42
56
55°
50°
45°
40°
35°
30°
25°
30°
25°
20°
15°
10°
5°
0°
5°
10°
15°
20°
25°
30°
35°
40°

Figure 6

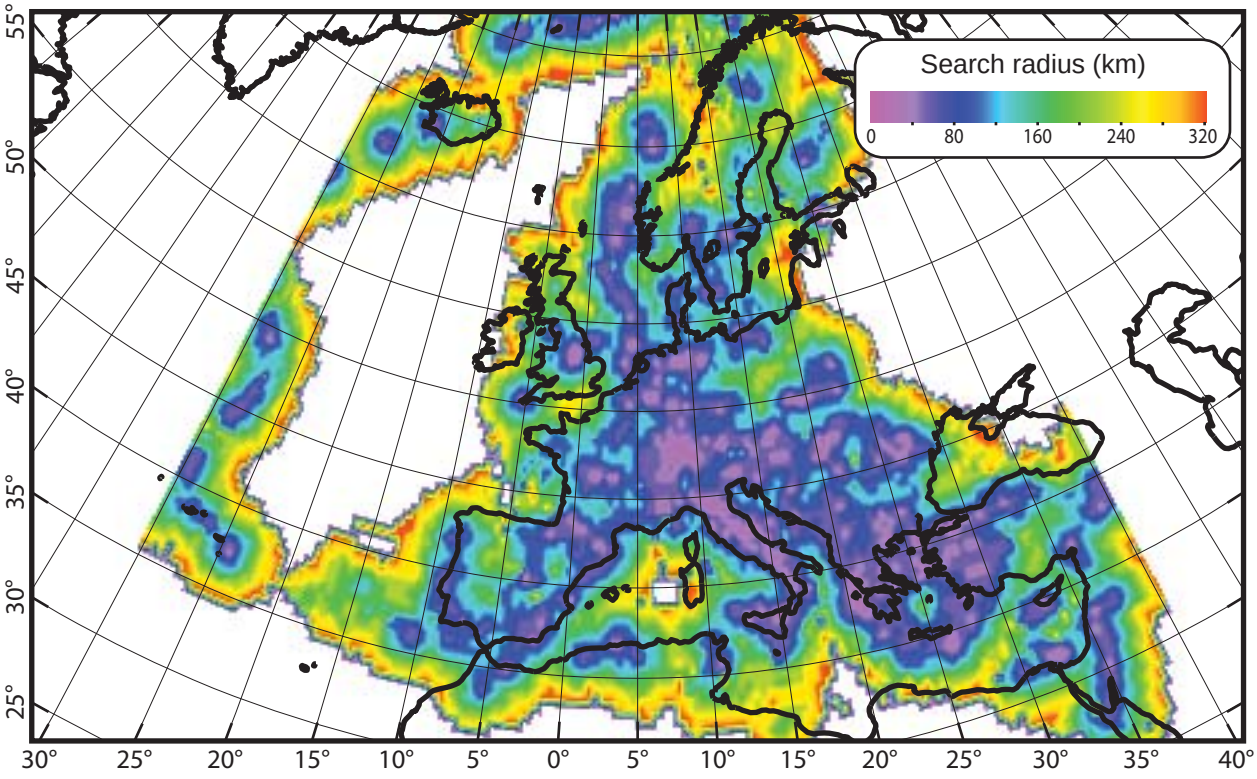
Search radius (km)
0
80
160
240
320
55°
50°
45°
40°
35°
30°
25°
30°
25°
20°
15°
10°
5°
0°
5°
10°
15°
20°
25°
30°
35°
40°

Figure 7

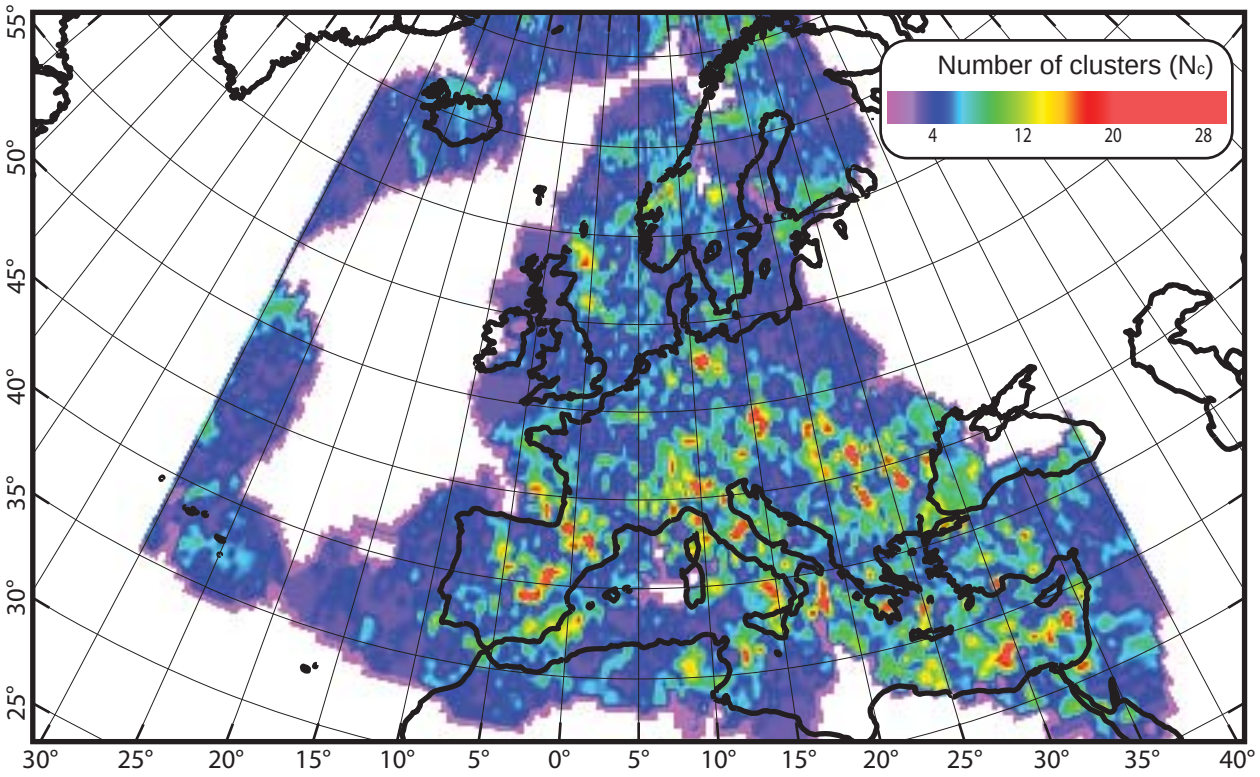
Number of clusters (Nc)
4
12
20
28
55°
50°
45°
40°
35°
30°
25°
30°
25°
20°
15°
10°
5°
0°
5°
10°
15°
20°
25°
30°
35°
40°

Figure 8a

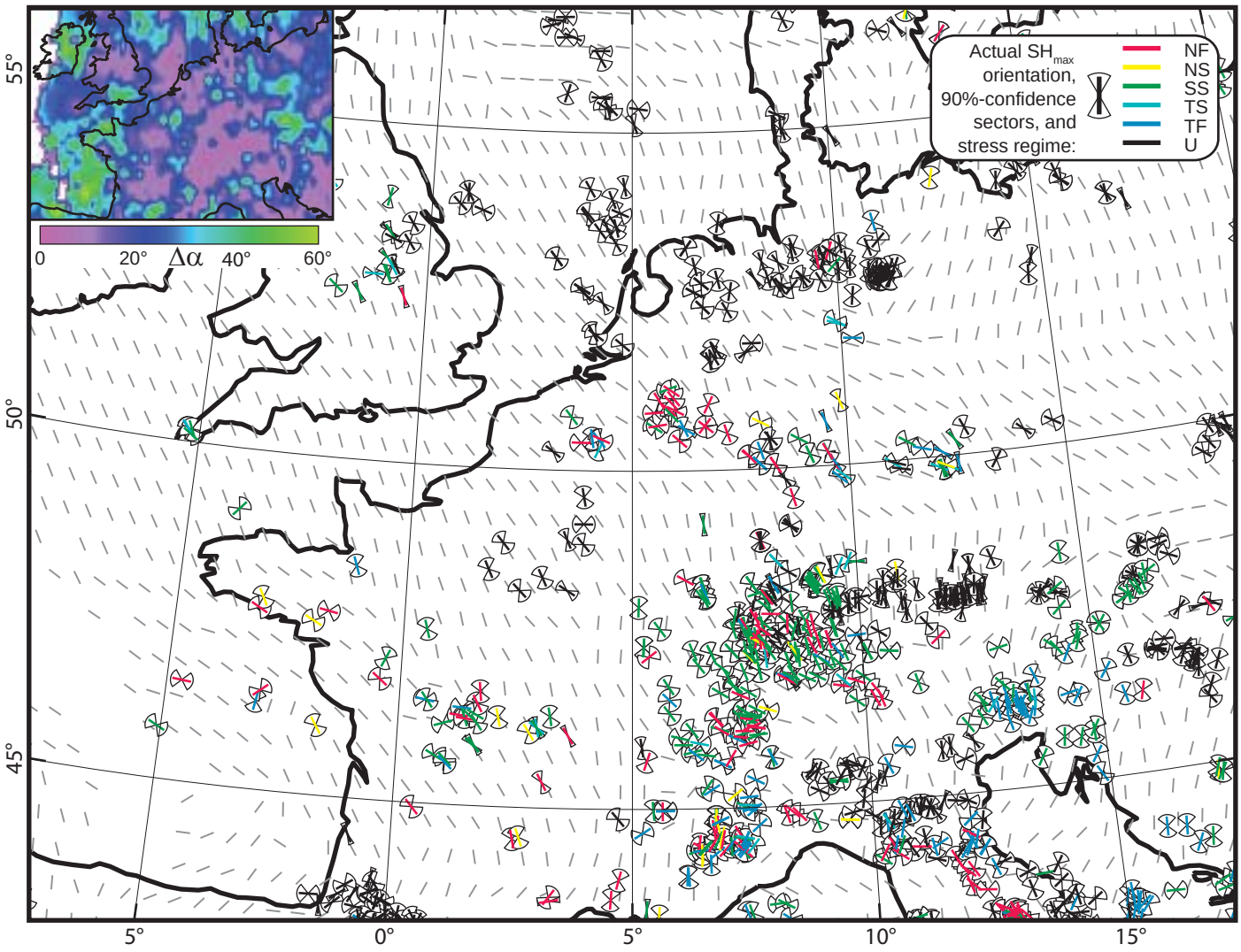
Actual SH$_{max}$ orientation, 90%-confidence sectors, and stress regime:
NF
NS
SS
TS
TF
U
0
20°
Δα
40°
60°
55°
50°
45°
5°
0°
5°
10°
15°

Figure 8b

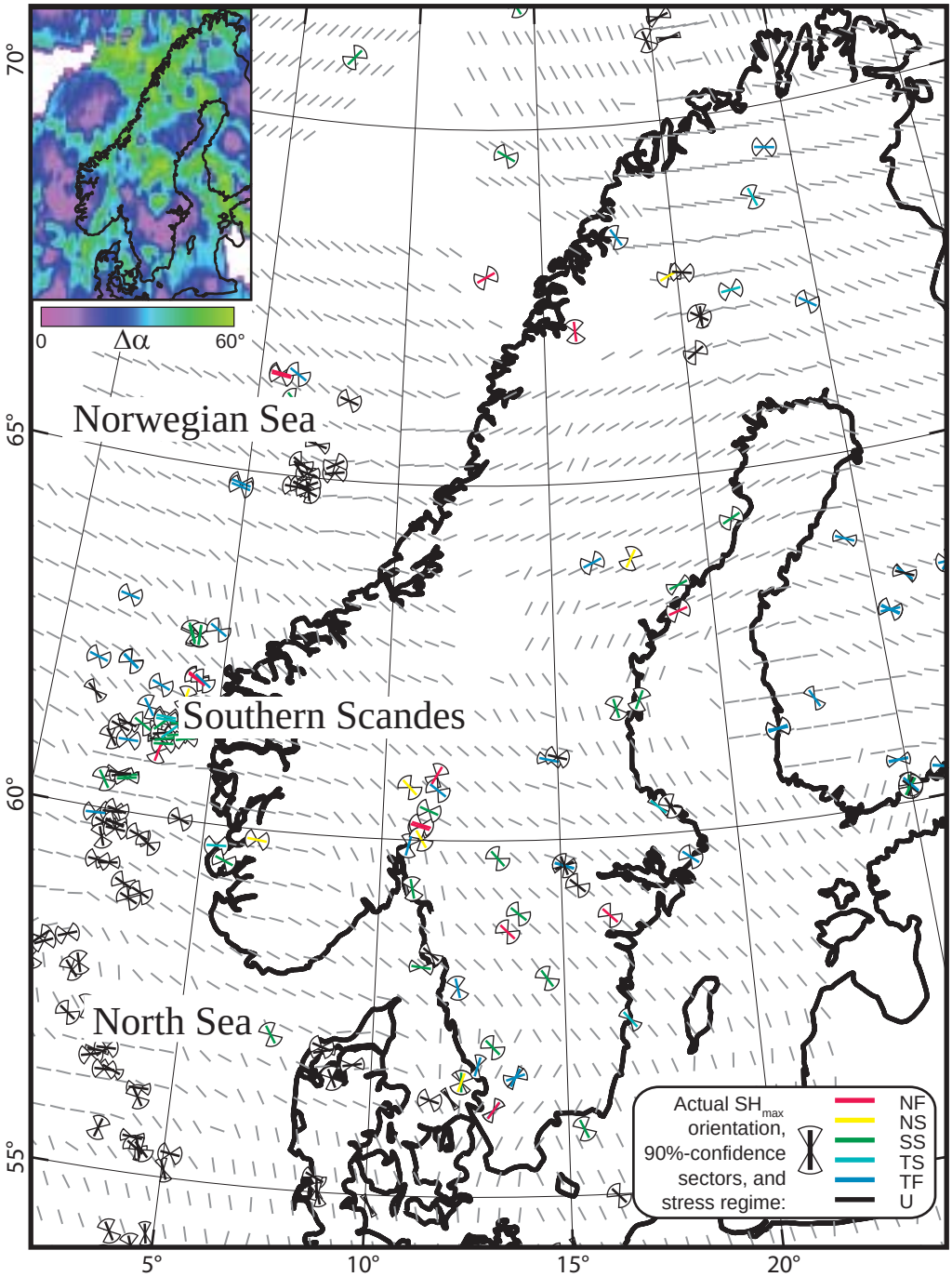
70°
65°
60°
55°
5°
10°
15°
20°
0
Δα
60°
Norwegian Sea
Southern Scandes
North Sea
Actual SH max orientation, 90%-confidence sectors, and stress regime:
NF
NS
SS
TS
TF
U

Figure 8c

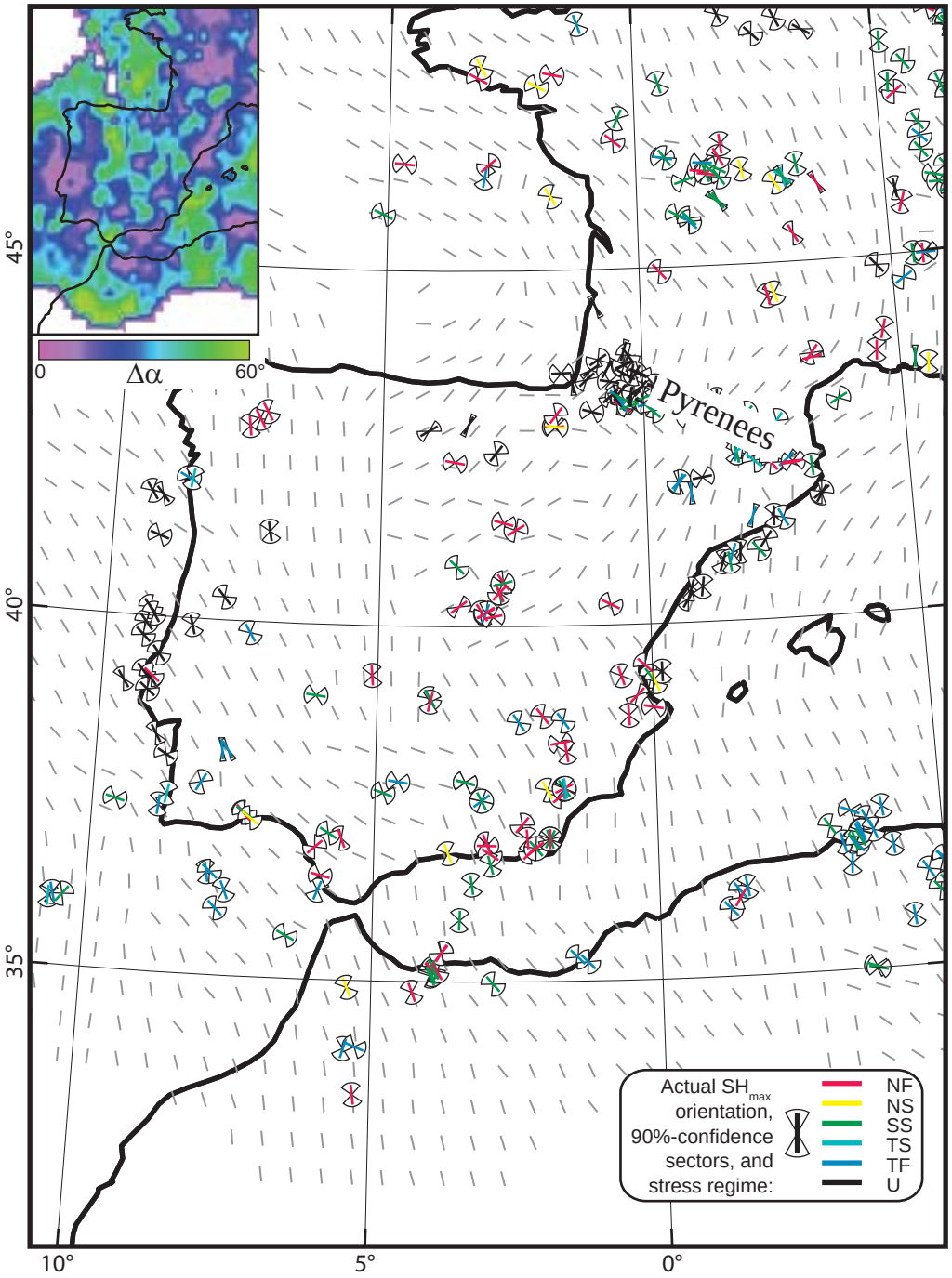
45°
40°
35°
10°
5°
0°
0
Δα
60°
Pyrenees
Actual SH max orientation, 90%-confidence sectors, and stress regime:
NF
NS
SS
TS
TF
U

Figure 8d

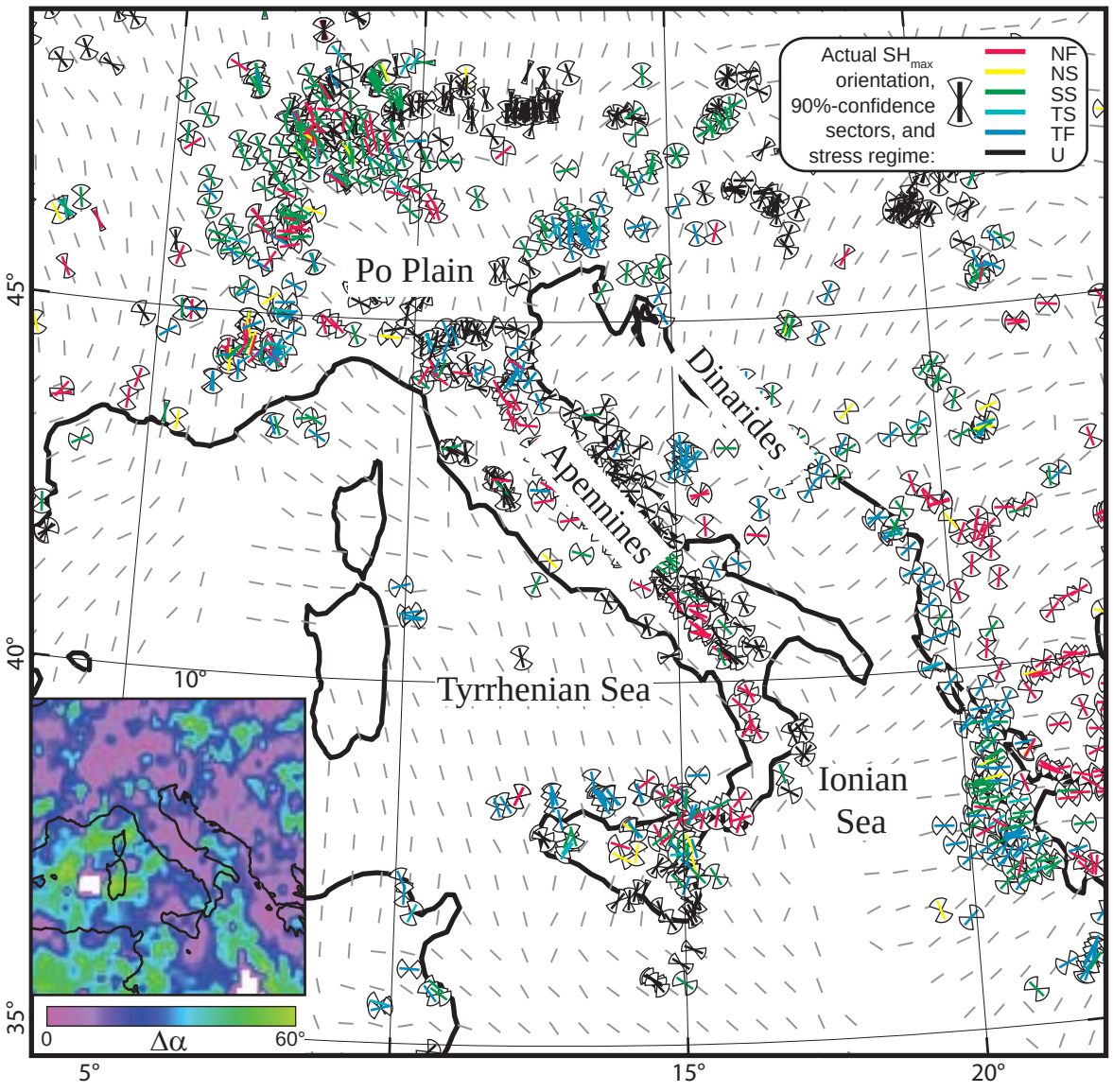
Actual SH$_{max}$ orientation, 90%-confidence sectors, and stress regime:
NF
NS
SS
TS
TF
U
Po Plain
Dinarides
Apennines
Tyrrhenian Sea
Ionian Sea
45°
40°
35°
10°
5°
15°
20°
0
Δα
60°

Figure 8e

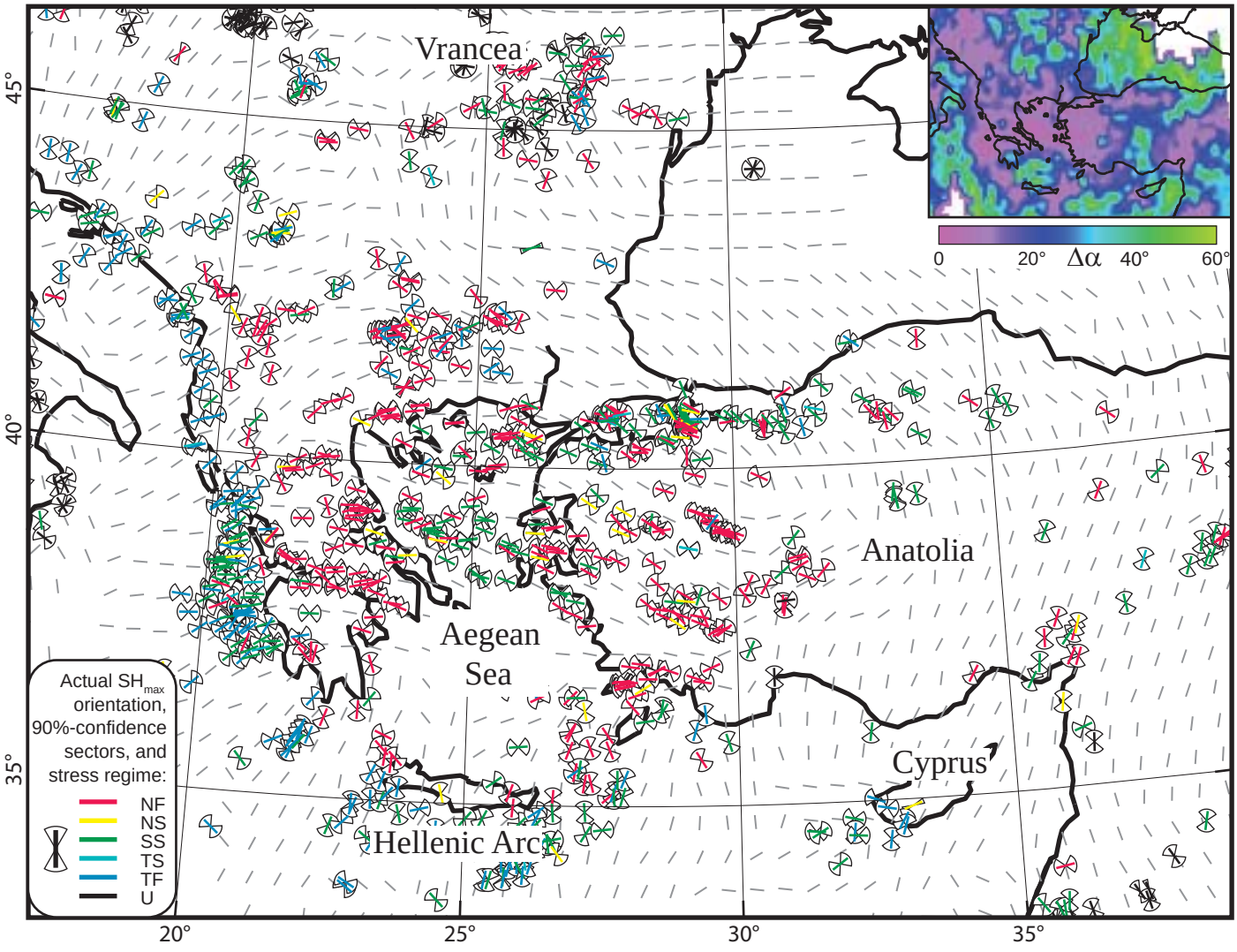
Vrancea
Anatolia
Aegean
Sea
Cyprus
Hellenic Arc
45°
40°
35°
20°
25°
30°
35°
0
20°
Δα
40°
60°
Actual SH$_{max}$ orientation, 90%-confidence sectors, and stress regime:
NF
NS
SS
TS
TF
U

Figure 9

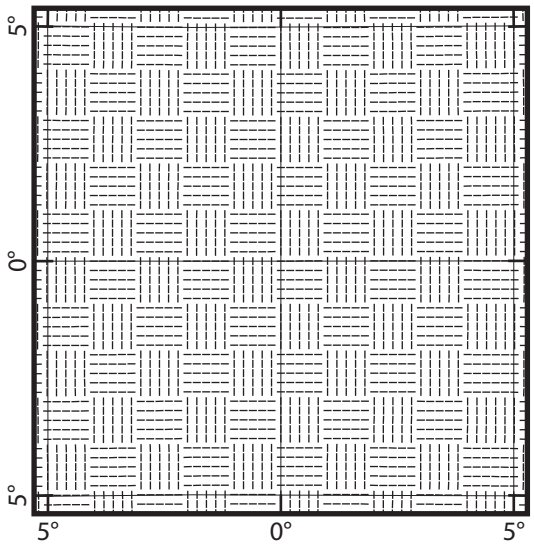

Figure 10

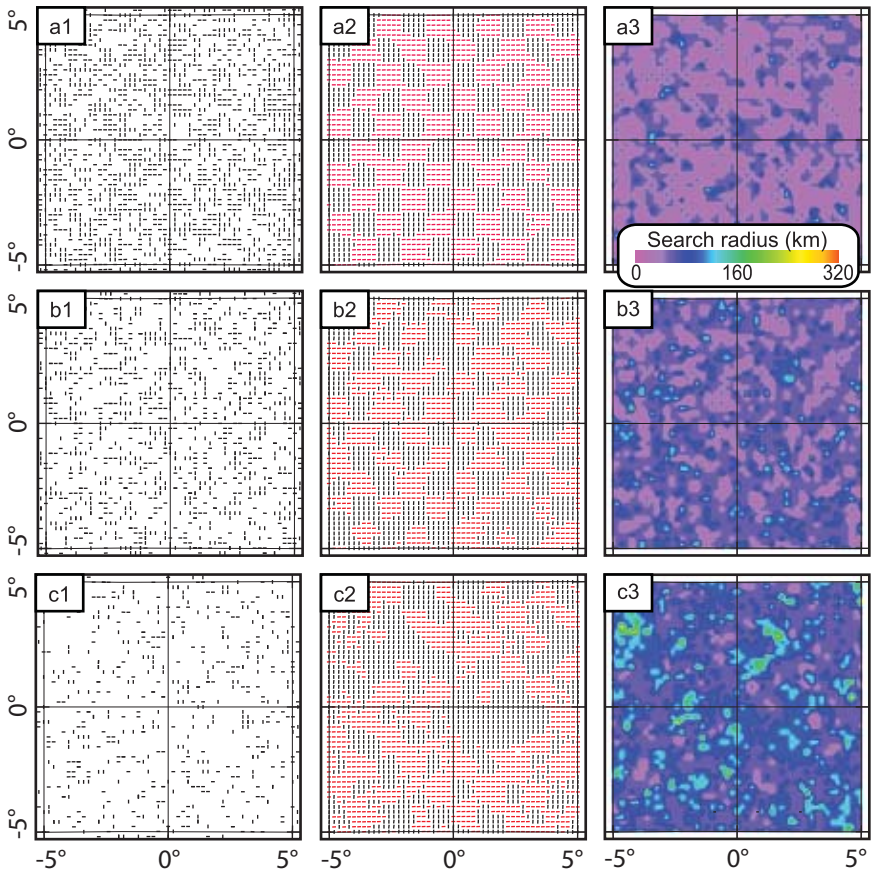

Figure 11

a)

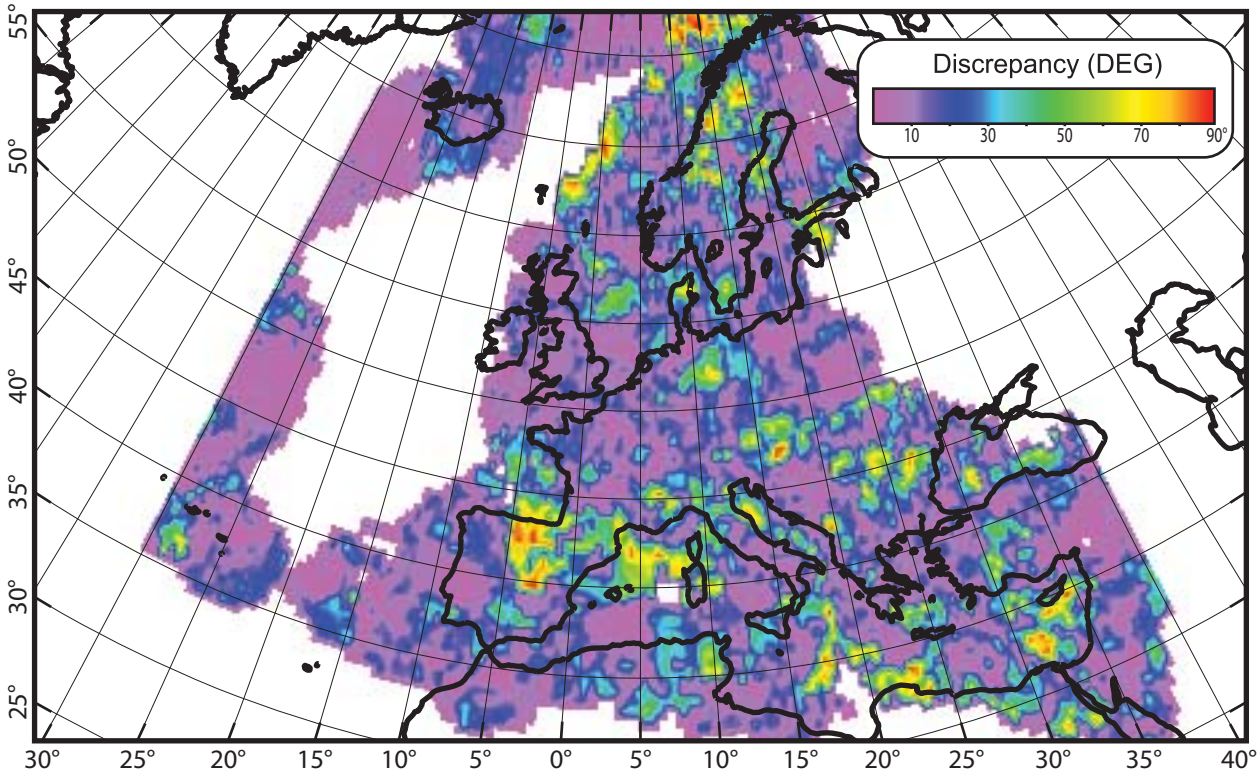
Discrepancy (DEG)
10
30
50
70
90°
55°
50°
45°
40°
35°
30°
25°
30°
25°
20°
15°
10°
5°
0°
5°
10°
15°
20°
25°
30°
35°
40°

b)

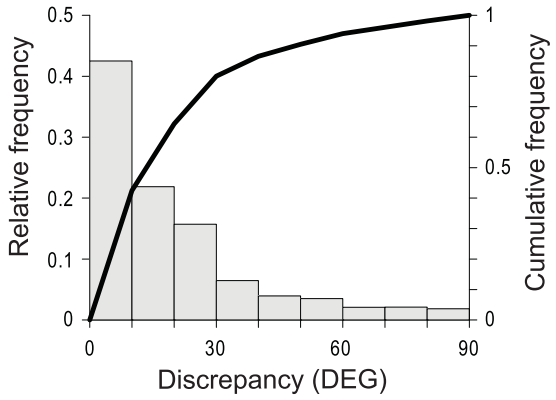
Relative frequency
Cumulative frequency
0.5
0.4
0.3
0.2
0.1
0
1
0.5
0
0
30
60
90
Discrepancy (DEG)

Figure 12

a)

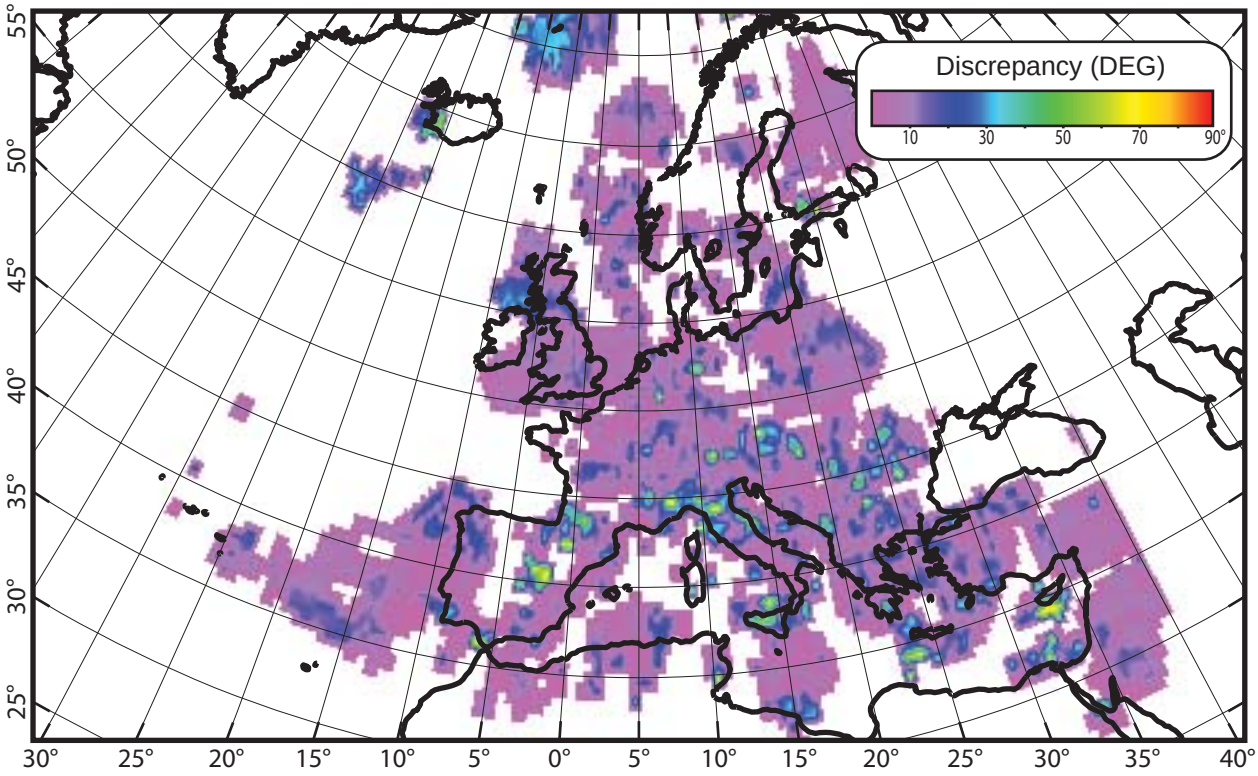
Discrepancy (DEG)
10
30
50
70
90°
55°
50°
45°
40°
35°
30°
25°
30°
25°
20°
15°
10°
5°
0°
5°
10°
15°
20°
25°
30°
35°
40°

b)

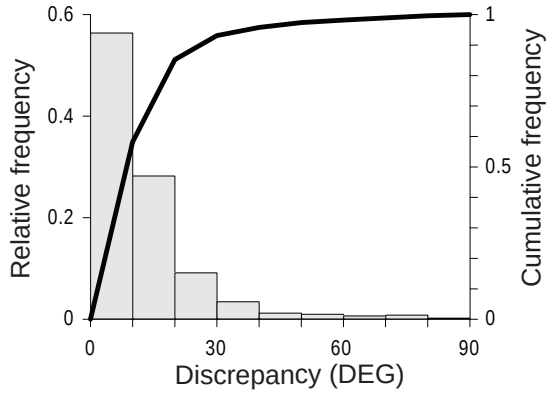
Relative frequency
Cumulative frequency
0.6
0.4
0.2
0
1
0.5
0
0
30
60
90
Discrepancy (DEG)

Figure 13

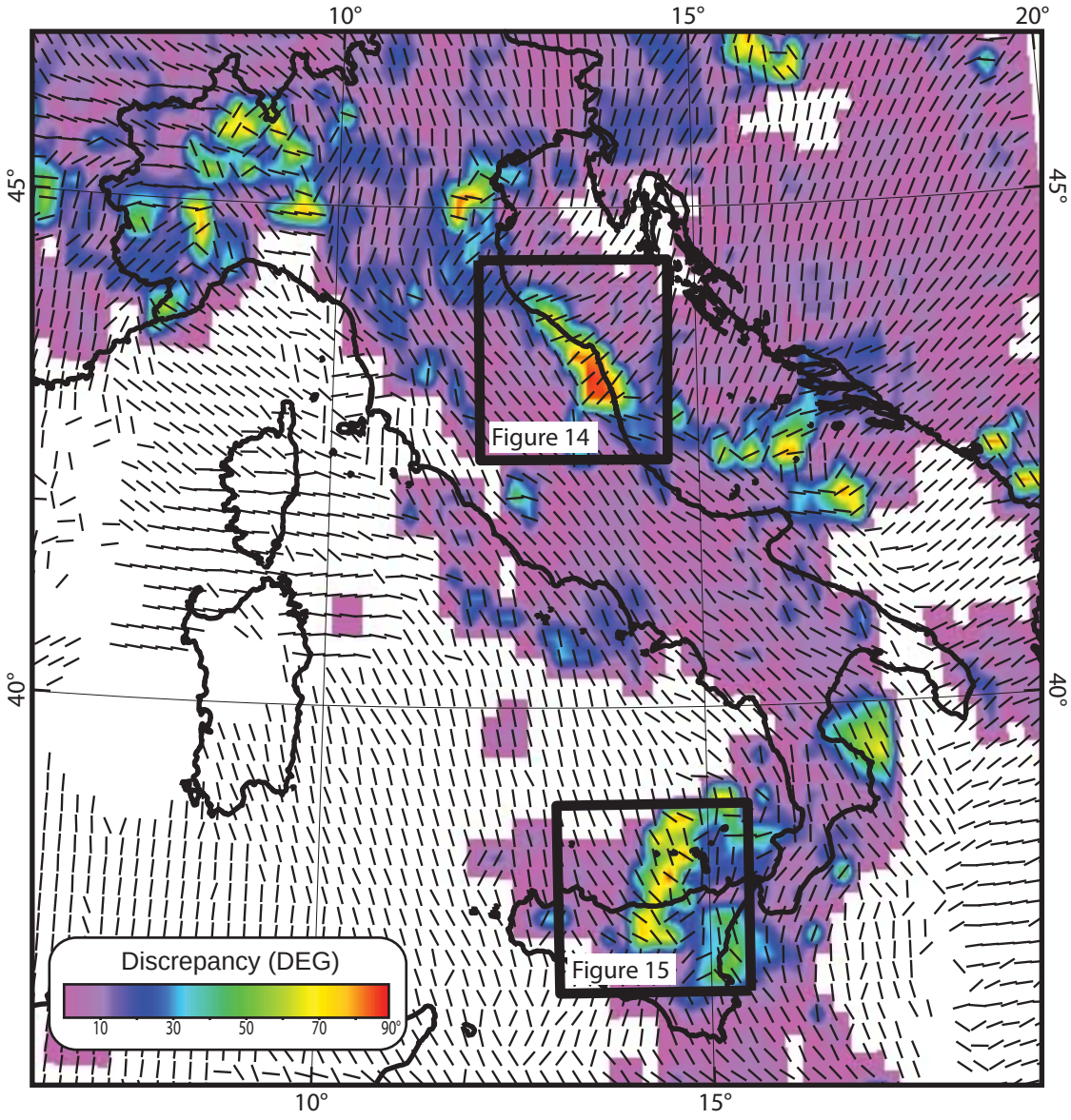
10°
15°
20°
45°
40°
Figure 14
Figure 15
Discrepancy (DEG)
10
30
50
70
90°

Figure 14

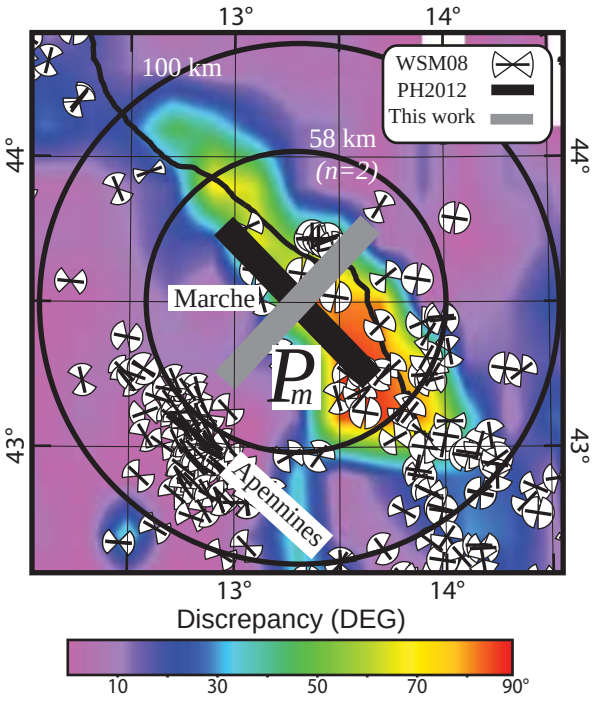
13°
14°
44°
43°
100 km
58 km
(n=2)
WSM08
PH2012
This work
Marche
Pm
Apennines
Discrepancy (DEG)
10
30
50
70
90°

Figure 15

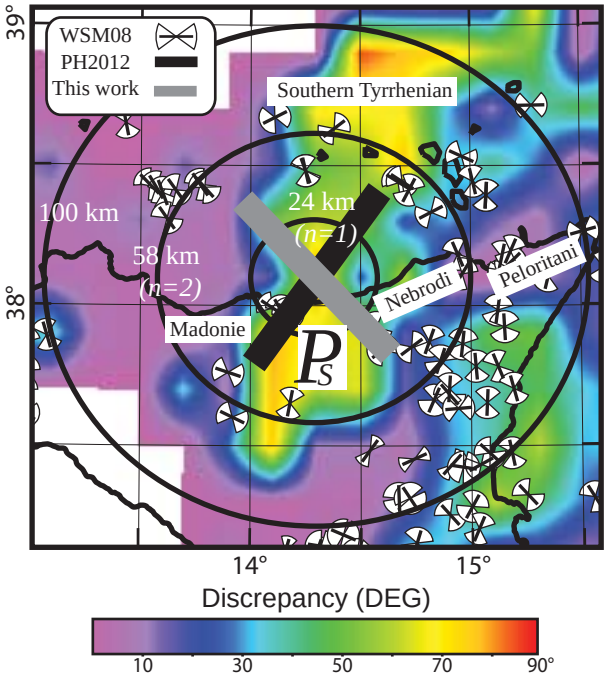
WSM08
PH2012
This work
Southern Tyrrhenian
24 km
(n=1)
100 km
58 km
(n=2)
Nebrodi
Peloritani
Madonie
Ps
39°
38°
14°
15°
Discrepancy (DEG)
10
30
50
70
90°

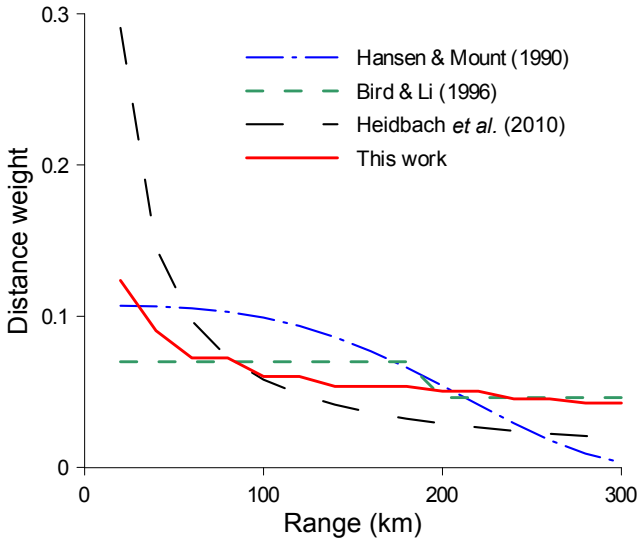
0.3
0.2
0.1
0
Distance weight
0
100
200
300
Range (km)
Hansen & Mount (1990)
Bird & Li (1996)
Heidbach *et al.* (2010)
This work

Figure 16

Figure A1

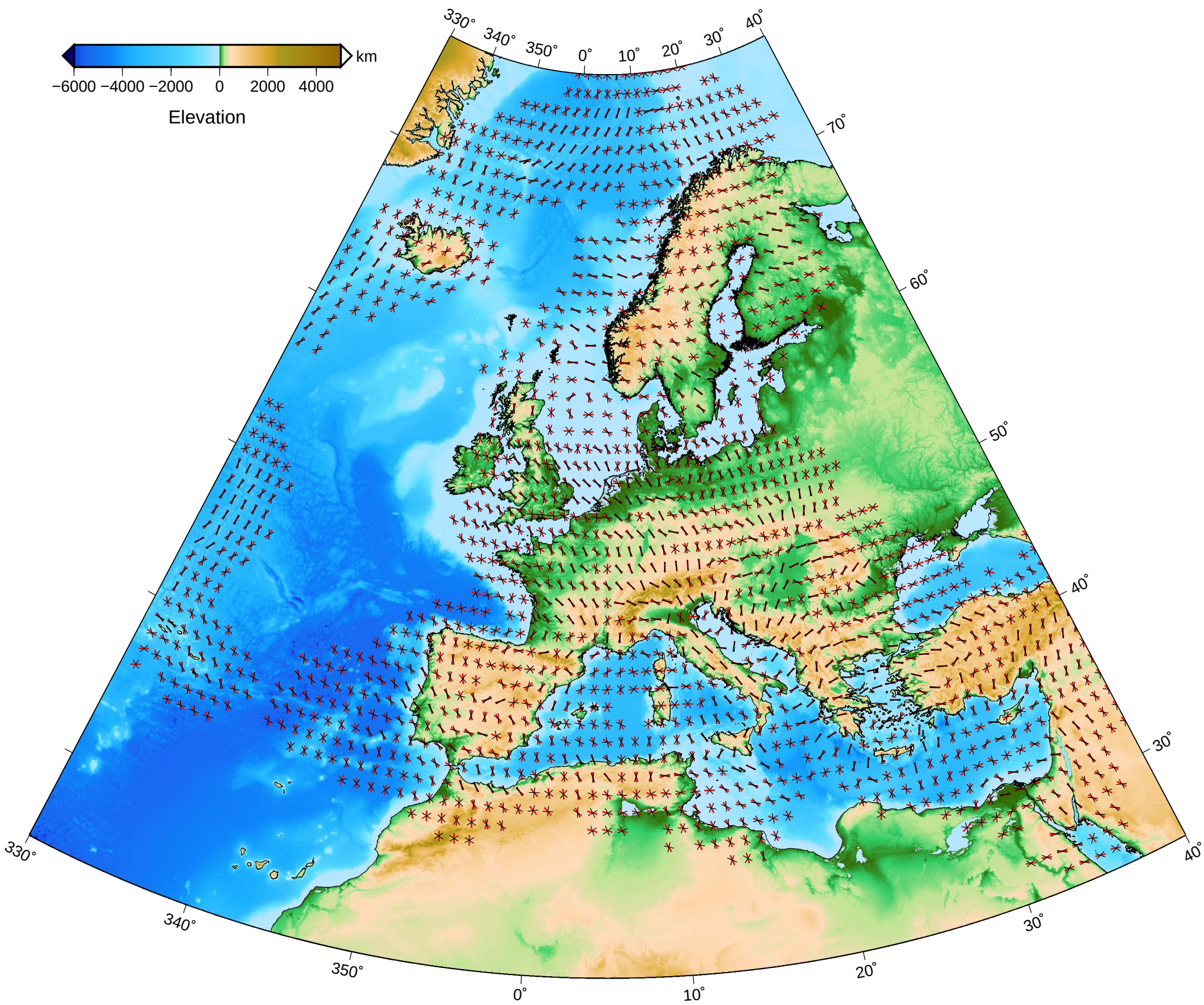
km
−6000 −4000 −2000 0 2000 4000
Elevation
330°
340°
350°
0°
10°
20°
30°
40°
70°
60°
50°
40°
30°
330°
340°
350°
0°
10°
20°
30°
40°